

(19) World Intellectual Property Organization
International Bureau



(43) International Publication Date
7 November 2002 (07.11.2002)

PCT

(10) International Publication Number
WO 02/088705 A2

(51) International Patent Classification⁷: **G01N 33/00**

Guillermo, J. [US/US]; 118 Kinnaird Steet Number 3, Cambridge, MA 02139 (US). **BOUMA, Brett, Eugene** [US/US]; 12 Monmouth Street, Quincy, MA 02171 (US).

(21) International Application Number: PCT/US02/13947

(22) International Filing Date: 1 May 2002 (01.05.2002)

(74) **Agent: BERNSTEIN, Jason, A.**; Bernstein & Associates, P.C., 6600 Peachtree Dunwoody Road, N.E., Embassy Row, Suite 495, Atlanta, GA (US).

(25) Filing Language: English

(26) Publication Language: English

(30) Priority Data:
60/287,899 1 May 2001 (01.05.2001) US

(81) **Designated States (national):** AE, AG, AL, AM, AT, AU, AZ, BA, BB, BG, BR, BY, BZ, CA, CH, CN, CO, CR, CU, CZ, DE, DK, DM, DZ, EC, EE, ES, FI, GB, GD, GE, GH, GM, HR, HU, ID, IL, IN, IS, JP, KE, KG, KP, KR, KZ, LC, LK, LR, LS, LT, LU, LV, MA, MD, MG, MK, MN, MW, MX, MZ, NO, NZ, OM, PH, PL, PT, RO, RU, SD, SE, SG, SI, SK, SL, TJ, TM, TN, TR, TT, TZ, UA, UG, US, UZ, VN, YU, ZA, ZM, ZW.

(71) **Applicant (for all designated States except US): THE GENERAL HOSPITAL CORPORATION** [—/—]; 55 Fruit Street, Boston, MA 02114 (US).

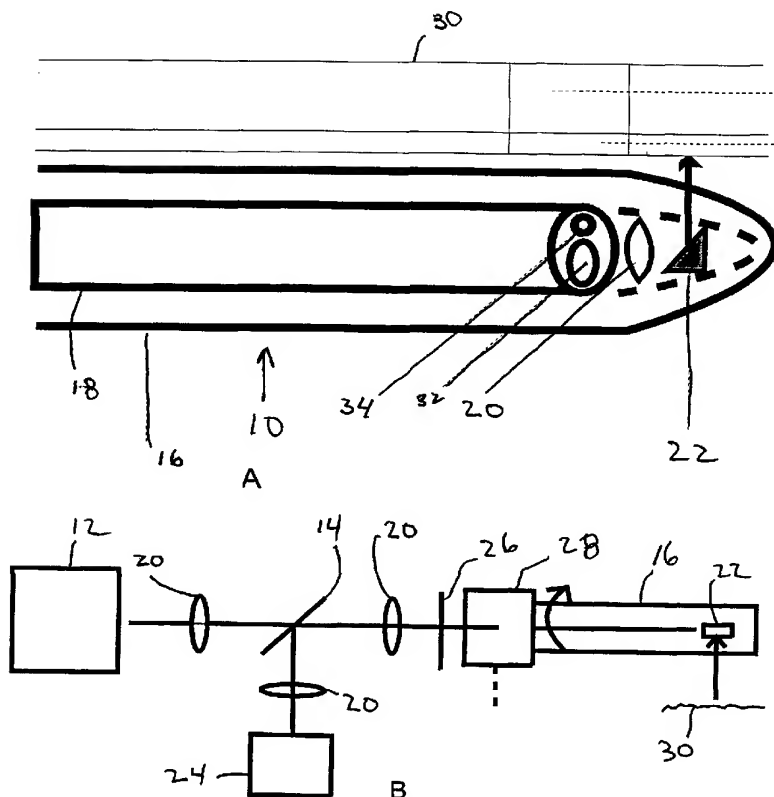
(84) **Designated States (regional):** ARIPO patent (GH, GM, KE, LS, MW, MZ, SD, SL, SZ, TZ, UG, ZM, ZW), Eurasian patent (AM, AZ, BY, KG, KZ, MD, RU, TJ, TM),

(72) Inventors; and

(75) Inventors/Applicants (for US only): **TEARNEY,**

[Continued on next page]

(54) **Title:** METHOD AND APPARATUS FOR DETERMINATION OF ATHEROSCLEROTIC PLAQUE TYPE BY MEASUREMENT OF TISSUE OPTICAL PROPERTIES



(57) **Abstract:** Methods for diagnosing vulnerable atherosclerotic plaque using optical coherence tomography to measure tissue optical properties, including backreflectance of heterogeneous layers, such as plaque cap, lipid pool composition and macrophage presence. Methods also include measurement of spatially and temporally dependent reflectance, measurement of multiple wavelength reflectance, low coherence interferometry, polarization and quantification of macrophage content.

WO 02/088705 A2



European patent (AT, BE, CH, CY, DE, DK, ES, FI, FR, GB, GR, IE, IT, LU, MC, NL, PT, SE, TR), OAPI patent (BF, BJ, CF, CG, CI, CM, GA, GN, GQ, GW, ML, MR, NE, SN, TD, TG).

For two-letter codes and other abbreviations, refer to the "Guidance Notes on Codes and Abbreviations" appearing at the beginning of each regular issue of the PCT Gazette.

Published:

— *without international search report and to be republished upon receipt of that report*

5

10

METHOD AND APPARATUS FOR DETERMINATION OF
ATHEROSCLEROTIC PLAQUE TYPE BY MEASUREMENT OF TISSUE
OPTICAL PROPERTIES

15

CROSS-REFERENCE TO RELATED APPLICATION

The present application claims priority from copending provisional application
20 number 60/287,899, filed May 1, 2001, and commonly assigned to the assignee of the
present application, and which is incorporated herein in its entirety.

FIELD OF THE INVENTION

The present invention provides methods for characterization of atherosclerotic plaque
by measurement of tissue optical properties, such as by optical coherence
25 tomography.

BACKGROUND OF THE INVENTION

Myocardial infarction is the major cause of death in industrialized countries. Rupture
of vulnerable atherosclerotic plaques is currently recognized as an important

mechanism for acute myocardial infarction, which often results in sudden death. Recent advances in cardiovascular research have identified anatomic, biomechanical, and molecular features of atherosclerotic plaques that predispose them to rupture. In a majority of vulnerable plaques, these features include 1) the presence of activated
5 macrophages at the shoulder or edge of the plaque, 2) a thin fibrous cap ($<60\mu\text{m}$) and 3) a large lipid pool. The lipid pool is thought to apply force to the fibrous cap that causes it to become compromised. Once it is ruptured, the lipid enters the vessel lumen, causing thrombosis, arterial occlusion, myocardial ischemia, and infarction. In addition to lipid-rich plaques with a thin fibrous cap, other plaque types have been
10 recently implicated as vulnerable plaques. These plaques contain a surface erosion where the intima has been denuded, leaving a rough surface at risk for causing platelet aggregation and acute thrombosis.

Coronary arteries that do not contain plaque have a layered structure consisting of an intima, media, and adventitia. A simple model of a lipid-rich plaque is a two layered
15 structure consisting of a fibrous cap and an underlying lipid pool. Other atherosclerotic plaque types consist of one layer, either fibrous or calcified. Research indicates that the distinct layers present in atherosclerotic plaques have different scattering, absorption, and anisotropy coefficients. It is believed that the measurement of these parameters using light will enable characterization of plaque type in vivo and
20 allow for the diagnosis of vulnerable plaques.

Cellularity of fibrous caps of atherosclerotic plaque, manifested by the infiltration of macrophages (average size 20-50 μm), is thought to weaken the structural integrity of the cap and predispose plaques to rupture. Macrophages, and other plaque related cells, produce proteolytic enzymes such as matrix metalloproteinases that digest

extracellular matrix and compromise the integrity of the fibrous cap. Activated macrophages are strongly colocalized with local thrombi in patients who have died of acute myocardial infarction and are more frequently demonstrated in coronary artery specimens obtained from patients suffering from acute coronary syndromes compared
5 with patients with stable angina. This evidence suggests that an imaging technology capable of identifying macrophages in patients would provide valuable information for assessing the likelihood of plaque rupture. Results from intracoronary OCT, recently performed in patients, have shown an improved capability for characterizing plaque microstructure compared with IVUS. To date, however, the use of OCT for
10 characterizing the cellular constituents of fibrous caps has not been fully investigated.

It would be desirable to have a means for using remitted light to measure the optical properties of atherosclerotic plaques, determine plaque cap thickness or identify plaques with surface erosions and as a result assess coronary plaque vulnerability.

A method that detects plaques vulnerable to rupture could become a valuable tool for
15 guiding management of patients at risk and may ultimately prevent acute events. Many different catheter-based methods are under investigation for the detection of vulnerable plaques. These methods include intravascular ultrasound (IVUS), optical coherence tomography (OCT), fluorescence spectroscopy, and infrared spectroscopy. While IVUS and OCT are used to obtain cross-sectional images of tissue, only OCT
20 has been shown to have sufficient resolution to detect the presence of a thin fibrous cap. Fluorescence and infrared spectroscopy are methods that primarily detect the presence of lipids within the vessel wall. Of the four proposed techniques, only OCT has been shown to be capable of spatially resolving parameters directly responsible for plaque rupture.

Background Principles

The backreflected light scattered from within a turbid medium, such as tissue, is affected by the optical properties of the medium. The optical properties that determine the propagation of light in tissue are the absorption coefficient, μ_a , the scattering
 5 coefficient, μ_s , and the total attenuation coefficient, μ_t , where

$$\mu_t = \mu_s + \mu_a$$

The absorption coefficient is linearly related to the concentration of the absorber, such that

$$\mu_a = \varepsilon[Ab]$$

10 where ε is the molar extinction coefficient for the absorber and $[Ab]$ is the molar concentration of the absorber.

Often, the mean cosine of the scattering phase function, g , is combined with μ_s to form the transport scattering coefficient:

$$\mu'_s = \mu_s(1 - g)$$

15 Propagation of light described using the transport scattering coefficient can be considered isotropic since the scattering coefficient has been normalized by the anisotropy coefficient, g .

Propagation of light within multiply scattering media is described by the radiative transport equation. Solutions to the radiative transport equation by use of diffusion
 20 theory approximations have allowed the use of remitted light to predict the optical

properties of homogeneous highly scattering media. Application of these techniques for diagnosing neoplasia has been problematic, however, due to tissue inhomogeneities and the large depth of tissue which must be probed to identify small tumors deeply embedded in tissue. Nevertheless, in the limited setting of atherosclerotic plaques, the tissue structure is less heterogeneous and the pathology is at the surface of the vessel. These two features of arterial pathology make characterization of atherosclerotic plaques by measurement of optical properties possible.

Figs. 1A and 1B show a schematic of the spatial remittance (r) for a fibrous plaque (Fig. 1A) and a lipid-rich plaque with a fibrous cap (Fig. 1B). The different optical properties of the two layers gives rise to a distinct remittance profile. This profile can be measured and the optical properties and thicknesses of the layers can be determined using two-layer diffusion approximation to the radiative transport equation. In Figs. 1A and 1B, a single beam of light is incident on the sample which is depicted as a two-layer model. Diffusion of light through the media produces a spatial remittance profile that is dependent on the optical properties of the media (Fig 1A). In Fig. 1B, i.e., the three-dimensional optical fluence is depicted as iso-contours. As can be seen in this simple schematic, the additional layer effects the spatially dependent three dimensional fluence and the remittance profile at the surface of the model. This effect is dependent on the optical properties and thicknesses of the layers and represents one method for measuring optical properties to characterize plaque composition and cap thickness. Fig. 2 shows the results of a preliminary study performed demonstrating the difference in radial remittance for different plaque types, in which Gaussian fits of the spatial remittance profiles were measured from a normal aorta and two lipid-rich plaques, one containing a thick fibrous cap and the other, a thin fibrous cap. The trend

towards decreasing remittance distribution width is a result of a decrease in the amount of light scattered from the fibrous cap ($\lambda = 633 \text{ nm}$).

SUMMARY OF THE INVENTION

The present invention describes methods for determining the fibrous cap thickness
5 and measuring tissue optical properties. In one embodiment of the present invention, the presence of a large lipid pool underlying the cap is measured. In another embodiment, macrophage degradation can be identified. Moreover, use of these techniques may allow determination of plaques containing surface erosions.

Several methods for measuring the optical properties of tissue can potentially be used
10 to investigate the structure of atherosclerotic plaques. Some of the methods described below may be modified, as is known to those skilled in the art, to incorporate multiple layers. These techniques may also be used as stand-alone measurements, or in combination.

Spatially dependent reflectance measurements

15 A single spot on the sample is irradiated with single or multiple wavelengths of light. The remitted light as a function of distance from the sample, r , is measured. Using the diffusion approximation and/or Monte Carlo simulation results, this radial remittance profile, combined with the total reflectance from the sample can yield the absorption and transport scattering coefficients of a homogenous medium. Recently, diffusion
20 theory has been used to calculate the optical properties of a two-layered media, and determine the layer thicknesses. In addition to the tissue optical properties, the cap thickness affects this spatial remittance distribution (Fig. 2F). Fitting experimentally measured spatial remittance distributions to Monte Carlo simulations (e.g., by the

Levenberg-Marquardt method) may allow for the determination of cap thickness for lipid-rich plaques.

Multiple wavelength reflectance measurements

5 Reflectance measurements may be made using two wavelengths with different penetration depths. If absorption for the two wavelengths is similar in atherosclerotic plaques, then the ratio of the reflectances for the two wavelengths gives an estimate of cap thickness.

Low-coherence interferometry (LCI)

10 Coherence ranging in tissue has been shown to be a powerful method for calculating the optical properties of layered tissue. Multiple linear fits of the LCI axial reflectivity allows determination of the total attenuation coefficient for each layer. Transitions between different linear fits determines the layer thicknesses of the tissue.

Quantification of Macrophage Content

15 The present invention provides methods for quantification of macrophage content of the cap. High macrophage content is indicative of potential plaque rupture. Several algorithms are presented for determining macrophage density, including, focus tracking, correction of focus, intensity normalization, computation of macrophage density within ROI, and cluster analysis or threshold application. OCT measures the intensity of light returning from within a sample. Samples having a higher
20 heterogeneity of optical index of refraction exhibit stronger optical scattering and therefore a stronger OCT signal. If the characteristic size scale of the index of refraction heterogeneity is larger than the resolution, then the OCT signal will have a larger variance. Previous research conducted to measure the optical properties of

human tissue has shown that the refractive index of lipid and collagen is significantly different. Caps containing macrophages should have multiple strong backreflections, resulting in a relatively high OCT signal variance.

5 A common theme to most of the methods described herein includes the use of a single fiber to irradiate the sample and multiple (small number) of fibers for detection. One embodiment of a catheter capable of making these measurements comprises a fiber optic array (one- or two-dimensional), lens, and prism which is contained within an inner housing capable of rotation. Light from one fiber input is focused by a lens, reflected off of a prism, and directed onto the artery wall. Light reflected from the
10 sample may be collected by other fibers in the fiber bundle. An image of the optical properties may be obtained by rotating the inner housing.. Since these techniques can be implemented using fiber optics, these measurements can be made using an intravascular device.

BRIEF DESCRIPTION OF THE DRAWINGS

15 The various features and advantages of the invention will be apparent from the attached drawings, in which like reference characters designate the same or similar parts throughout the figures, and in which:

Fig. 1A is a schematic of the spatial remittance (r) for a fibrous plaque . Fig. 1A is the path of average photons which is affected by the scattering, absorption, and anisotropy coefficient Fig. 1B is a schematic of the spatial remittance (r) for a lipid-rich plaque
20 with a fibrous cap. Fig. 1B is a cross-sectional view of the three-dimensional fluence (as an isocontour plot).

Fig. 2 shows Gaussian fits of the spatial remittance profiles measured from a normal aorta and two lipid-rich plaques, one containing a thick fibrous cap and the other, a thin fibrous cap.

Fig. 3 is a Monte Carlo simulation of radial remittance.

5 Fig. 4A is a graph of an incoming short temporal pulse.

Fig. 4B is a graph of an outgoing pulse with decay and broadening of the pulse.

Fig. 4C is a graph of an outgoing pulse reflecting off a cap with a lipid pool showing two decay curve slopes.

10 Figs. 5A and B are schematic views of a generalized catheter and detector system according to an embodiment of the present invention.

Fig. 5C is a schematic view of a system having a short pulse light source and a time gated electronic.

Fig. 6A and B show graphs of oscillating light at different amplitudes A_1 and A_2 .

15 Fig. 7A cap thickness as a function of frequency (F) where two peaks A_{LP} (amplitude of the lipid pool) and A_{CAP} (amplitude of the cap) are related to the optical properties.

Fig. 7B shows a phase plot of the angle F as a function of ϕ in radians and is also dependent on cap thickness and optical properties.

Fig. 8 is a schematic view of an alternative embodiment of a system of the present invention.

Fig. 9 shows Monte Carlo wavelength ratiometric spatial reflectance distributions for two different cap thicknesses.

Fig. 10A is a histogram or probability distribution function (PDF) for different tissue regions.

5 Fig. 10B is an OCT image containing a lipid-rich region, a calcification, and a fibrous cap.

Fig. 10C is an OCT image showing a fibrous cap and a lipid pool with different total attenuation coefficients.

10 Fig. 10D is an OCT image of a large intimal calcification has a higher total attenuation coefficient than either the fibrous cap or lipid pool in Fig. 10C.

Fig. 11 shows a schematic of a polarization sensitive OCT system according to one embodiment of the present invention.

Fig. 12A and B shows OCT images of human coronary artery plaque acquired in vivo. A. Polarization independent image shows the presence of a fibrous plaque from 11 o'clock to 8 o'clock (clockwise). B. Polarization sensitive image shows presence of bands (arrows) within the fibrous plaque.

15

Figs. 13A-C show images taken using polarization sensitive OCT. Fig. 13A is an OCT polarization diversity image; Fig. 13B is a polarization sensitive image; and, Fig. 13C is the histology of the same site.

20 Figs. 14. A and B are graphs showing the correlation between the Raw (A) and logarithm base 10 (B) OCT NSD and CD68% area staining (diamonds - NSD data; solid line - linear fit).

DETAILED DESCRIPTION OF THE EMBODIMENTS

SPATIALLY DEPENDENT REFLECTANCE

Figs. 1A and B are schematic illustrations of the spatial remittance. Fig. 2 is a graph of spatial remittance profiles that were experimentally obtained from aortic
5 atherosclerotic plaques in vitro. Both figures are an experimental fit of shining light in (wavelength is 633 nm) and looking at the light coming out (spatial remittance distribution) using a CCD array. Fig. 2 shows Gaussian fits of the spatial remittance profiles measured from a normal aorta and two lipid-rich plaques, one containing a thick fibrous cap and the other, a thin fibrous cap. The trend towards decreasing
10 remittance distribution width is a result of a decrease in the amount of light scattered from the fibrous cap ($\lambda = 633$ nm). Fig. 2 shows the light entering at distance = 0 and remittance is graphed as a function of distance from where the light went into the cap. The solid line is a normal aorta; the dotted line is thick cap plaque (about 150 micrometers); and the dashed line is thin cap plaque (about 40 micrometers). The
15 concept is that the optical properties are different in the lipid pool than in the cap so when light is incident on a thick cap plaque, the spatial reflectivity profile is primarily affected by the cap optical properties. For thinner caps, the spatial reflectivity is more dependent on the lipid optical properties. In other words, for thick cap plaques, the spatial reflectance profile more closely resembles spatial reflectance from a fibrous
20 layer of semi-infinite thickness, whereas for a thin cap plaque, the spatial reflectance profile more closely resembles the spatial reflectance from a semi-infinite lipid pool. This technique may be enhanced by selecting wavelengths (e.g., 450- 500 nm, 1050-1350 nm, and 1600-1850 nm) which are preferentially absorbed by lipid.

There have been prior attempts to measure the optical properties of human atheromas, but these studies suffer from a number of deficiencies and inaccuracies. In addition, the unique optical properties of atherosclerotic caps and lipid pools have not been independently measured.

- 5 Table 1 shows the optical properties of the cap and lipid pool (literature and unpublished research) used for Monte Carlo simulations at 633 nm and 476 nm.

TABLE 1A - CAP

633 nm	476 nm
$M_a=3.6 \text{ cm}^{-1}$	$M_a=14.8 \text{ cm}^{-1}$
$M_s=171 \text{ cm}^{-1}$	$M_s=237 \text{ cm}^{-1}$
$g=.85$	$g=.85$

TABLE 1B – LIPID POOL

633 nm	476 nm
$M_a=3.6 \text{ cm}^{-1}$	$M_a=45 \text{ cm}^{-1}$
$M_s=870 \text{ cm}^{-1}$	$M_s=1200 \text{ cm}^{-1}$
$g=.95$	$g=.95$

10

Fig. 3 shows the results of a Monte Carlo simulation (a “random walk” technique known to those skilled in the art) of radial remittance (distance in mm) as a function of remittance or reflectance (a.u.). The solid line represents the radial remittance at 476 nm for a thick cap (150 micrometers) and the dashed line is for a thin cap (65 micrometers). The spatially dependent reflectance for the thin cap model is lower than that of the thick cap plaque due to the increased fluence in the lipid pool and resultant increased absorption.

15

Multiple wavelengths may be used to improve the accuracy of this technique. Spatial reflectance measurements may be obtained for a sufficient number of wavelengths to solve for the multiple degrees of freedom present in the N-layered model. Variables that need to be determined to accurately determine the cap thickness include the
 5 absorption coefficient, the transport scattering coefficients for each layer and the layer thickness.

One method according to the present invention for measurement of plaque optical properties and cap thickness is as follows:

- 1) Perform Monte Carlo simulations varying cap and lipid pool optical properties
 10 and cap thicknesses;
- 2) Develop a lookup table of Monte Carlo results;
- 3) Perform spatial reflectance distribution measurements for N wavelengths;
- 4) Fit the measured spatial reflectance distribution to known Monte Carlo simulation results (e.g., by the Levenberg-Marquardt method); and,
- 15 5) Output the optical properties and cap thickness from the previously computed Monte Carlo simulation that closely approximates the experimental measurements

TIME DEPENDENCE

Fig. 4A(i) shows a graph of a short temporal pulse going in and Fig. 4B shows a graph
 20 of the decay and broadening of the pulse coming out, which allows the measurement of the effective attenuation coefficient: $\mu_{\text{eff}} = 1/[3\mu_s(\mu_s + \mu_a)]$ or the total attenuation coefficient, $\mu_t = \mu_s + \mu_a$, where μ_t is the total scattering coefficient, μ_a is the absorption

coefficient, and μ_s is the scattering coefficient. Fig. 4B is indicative of a liquid pool where a pulse enters and is broadened by effects of the optical properties of the cap and the lipid pool, causing the decay curve to change. For a two-layered structure, there will be a superposition of two decay curves, one due to the optical properties of the cap, and the other due to the optical properties of the lipid pool. So, in Fig. 4C there are two decay curves, the left most slope "1", is $e^{-\mu_1 t}$ is due to the cap alone and the right most slope "2", is $e^{-\mu_2 t}$ is due to the cap plus lipid pool. In this graph $\mu_1 = \mu_c$ cap and $\mu_2 = \mu_c$ cap + liquid. Determination of the cutoff region where the exponential decay changes allows for the measurement of cap thickness.

10 Figs. 5A and 5B are schematic illustrations of a generalized view of a catheter 10 which comprises a light source 12, a beam splitter 14, a probe 16, a fiber 18, a lens 20 (optional), a reflecting element 22 (which is optional; alternatively, it can go straight through the catheter 10), a detector 24 (such as, but not limited to, a CCD, one dimensional array, two dimensional array, and the like), an optional polarizer 26, 15 rotational coupler 28, and a sample 30. There is a coupler 28 at the proximal end of the catheter device 10 which may rotate or translate the incident beam of light to perform cross-sectional or longitudinal imaging of the vessel optical properties. It is also possible to have an image fiber 32 bundle which can rotate. Also, there optionally can be an irradiant port 34. Optionally, there can be a plurality of lenses 20 or at least one polarizing filter 36 (not shown), depending on which imaging method is to be 20 used.

Fig. 5C shows a schematic of a system 50 having a short pulse source 52, which passes a light beam 54 into the beam splitter 55 (BS), into and back out of the probe 56. The system 50 includes a time gated electronic 58, known to those skilled in the

art; for example, but not by way of limitation, a Kerr lens 60, a streak camera, high speed photodiode detector, or the like.

Figs. 6A and 6B show graphs where instead of putting a pulse of light in, one uses an oscillating light in at amplitude A_1 and out at amplitude A_2 , where a phase shift
5 (ϕ) occurs between the two peaks in Fig. 6A and 6B and there is an amplitude decrease where $A_2 < A_1$.

Fig. 7A shows cap thickness as a function of frequency (F) where two peaks A_{LP} (amplitude of the lipid pool) and A_{CAP} (amplitude of the cap) are related to the optical properties. Fig. 7B shows a phase plot of the angle F as a function of ϕ in radians and
10 is also dependent on cap thickness and optical properties.

Fig. 8 shows a schematic of an alternative embodiment of a system 70 having a light source 72, a modulator 74, a beam splitter 76, and a probe 78. There is also a demodulator 80, either optical or electronic, and a detector 82.

One can also combine spatial frequency and spatial time and/or modulated phase and
15 amplitude measurements.

MULTIPLE WAVELENGTH REFLECTANCE MEASUREMENTS

The use of the differential penetration depth of light within the fibrous cap provides a simple method for estimating cap thickness. This technique may be performed using a single point measurement or for multiple points as a spatially dependent reflectance
20 profile (as mentioned above). The principle behind this method is illustrated by the following aspects:

- 1) λ_1 has a lower wavelength and a resultant decreased penetration depth.

- 2) λ_2 has a higher wavelength and a resultant increased penetration depth.
- 3) Both λ_1 and λ_2 are absorbed by lipid and predominantly scattered by the cap (see wavelengths discussed above).
- 4) If the cap is thin, then the reflectance ($I\lambda_1$) is higher than $I\lambda_2$ and the ratio, $R = I\lambda_1/I\lambda_2$ is high. This is due to the fact that λ_1 light is scattered back to the detector before it is absorbed, whereas the λ_2 light penetrates the cap and is absorbed.
- 5) If the cap is thick, then the reflectance ($I\lambda_1$) is roughly equal to $I\lambda_2$ and the ratio, $R = I\lambda_1/I\lambda_2 \approx K_2$. Also, each individual $I\lambda_1$ and $I\lambda_2$ are high.
- 6) If the cap is very thin (i.e., indicating likely vulnerable plaque), then both wavelengths penetrate the cap, the ratio, $R = I\lambda_1/I\lambda_2 \approx K_1$, and each individual $I\lambda_1$ and $I\lambda_2$ are relatively low.
- 7) Additional wavelengths and/or spatial reflectance measurements may be used to increase the accuracy of this technique.

Fig. 9 shows Monte Carlo wavelength ratiometric spatial reflectance distributions for two different cap thicknesses. For this simulation, the maximum difference between ratios for the two cap thickness (65 μm and 150 μm) occurs at a source detector separation of $d=200 \mu\text{m}$. This simulation shows that the sensitivity of this technique may be improved using spatial reflectance measurements (e.g., source and detector locations separated by a distance d).

There are multiple different wavelength ratiometric equations, including, but not limited to:

$$(1) \quad R = I\lambda_1/I\lambda_2$$

$$(2) \quad R = (I\lambda_1 - I\lambda_2) / (I\lambda_1 + I\lambda_2)$$

$$(3) \quad R = I\lambda_1 / (I\lambda_1 + I\lambda_2)$$

$$(4) \quad R = (I\lambda_1 - I\lambda_2) / I\lambda_2$$

The appropriateness of the equation depends on whether or not the total reflectance
5 needs to be accounted for (normalized) to correct for intrapatient and interpatient
variation of the cap and lipid pool optical properties.

LOW COHERENCE INTERFEROMETRY

Low coherence interferometric imaging or optical coherence tomography is a non-
invasive cross-sectional imaging technique capable of providing high-resolution
10 images of optical backscattering within tissue. OCT is currently being developed as a
commercial product and will likely begin wide-scale clinical trials in the coming
years. Current OCT systems have a resolution of 10 μm . Although this resolution
allows for imaging of tissue architectural morphology, cellular features are not
directly resolved by OCT. As a result, quantitative/qualitative algorithms must be
15 used to correlate architectural features visualized by OCT to identify coronary
atherosclerotic plaque type.

Interpretation of OCT images is based on several hypotheses that are directly
supported by clinical experience:

1. OCT signal strength increases with nuclear (N) density
- 20 2. OCT signal strength increases with fibrous tissue density
3. Lipid exhibits a low OCT signal

4. Calcifium may exhibit a low or high (or alternating low and high) OCT signal
 5. The refractive indices of fibrous tissue, lipid, and calcium are distinct. As a result, for well-delineated structures, a high OCT signal (Fresnel reflection) may be observed at the interface between different tissue types.
- 5 An algorithm for feature extraction from OCT images is described below. Final diagnosis of coronary pathology can be determined using a grading scheme incorporating some or all of the parameters described herein.

Qualitative features

Table 2

Histopathologic Finding	OCT Features
Intimal hyperplasia	Signal-rich layer nearest lumen
Media	Signal-poor middle layer
Adventitia	Signal-rich, heterogeneous outer layer
Internal elastic lamina	Signal-rich band (~20 μ m) between the intima and media
External elastic lamina	Signal-rich band (~20 μ m) between the media and adventitia
Atherosclerotic plaque	Loss of layered appearance, narrowing of lumen
Fibrous tissue	Homogeneous, signal-rich region
Lipid pool	Heterogeneous, poorly delineated, signal-poor (echolucent region)
Fibrous cap	Signal-rich band overlying echolucent region
Macrocalcification	Large, heterogeneous, sharply delineated, signal-poor or signal-rich region
Microcalcification	Punctate high-signal region
Dissections	Intimal/medial defect
Thrombus	Homogeneous, well-defined structure adherent to luminal surface protruding into vessel lumen

10

Table 2 describes the OCT qualitative features corresponding to histologic finding.

Table 2 partially overlaps with published data. However, many OCT features described in Table 2 have not been mentioned in the literature.

We have also recently noted two types of lipid pools, homogeneous and heterogeneous. Homogeneous lipid pools have a greatly decreased signal and contain a Fresnel reflection at the interface. Heterogeneous lipid pools have increased signal compared to homogeneous lipid pools and do not have a visible Fresnel reflection.

5 Quantitative Features

While many cross-sectional OCT images of human coronary arteries can be readily characterized using simple, qualitative features, heterogeneous plaques with complex components are difficult to interpret. In these cases, the appearance of lipid-rich plaques with thin fibrous caps was similar to that of fibrous plaques with
 10 calcifications. To date, few investigators have used advanced image processing algorithms for OCT. Preliminary studies suggest that substantial improvements can be made in identifying tissue constituents through systematic analysis of the two-dimensional OCT signal and that algorithms can be developed for applying this information for contrast enhancement and segmentation.

15 In current OCT systems, the intensity of light returning from discrete locations within the sample comprises the image data set. The signal detected from any one location is determined by both the attenuation incurred along the optical path between the catheter and the location and the actual reflectivity at that location, $R(z)$:

$$I(z) = I_0 R(z) \int e^{-2\mu_t(z)z} dz, \quad \text{Eq. 1}$$

20 where I_0 is the incident light intensity, μ_t is the total attenuation coefficient and z is the distance along the optical axis. As light propagates within tissue it is attenuated by scattering and absorption. In a homogeneous medium, the total attenuation coefficient is independent of depth resulting in a single-exponential decay of signal with depth. In

more complex structures the spatial dependence of the attenuation coefficient gives rise to an exponential decay curve with locally varying slope.

Recent work in our laboratory has shown that OCT data representing different components of plaques have distinct local intensity distributions. This realization has motivated the use of three methods for quantitative analysis and segmentation of OCT data representing different tissue types. Computation of the histograms or probability distribution functions (PDF) for different tissue regions has shown that each tissue type has a distinct PDF (Fig. 10), making it likely that local PDF statistics such as the mean, standard deviation and skew could be used for image segmentation. Next, preliminary analysis of existing data shows that separate plaque components have different local spatial frequency distributions or textures. Due to the fractal nature of biological tissue, the fractal dimension (D) was chosen as a quantitative measure of local texture in OCT images. Fig. 10B is an OCT image containing a lipid-rich region, a calcification, and a fibrous cap. Following processing, each different plaque component was found to have a distinct fractal dimension (D). Fig. 10C is an OCT image showing a fibrous cap and a lipid pool with different total attenuation coefficients. Fig. 10D is an OCT image of a large intimal calcification has a higher total attenuation coefficient than either the fibrous cap or lipid pool in Fig. 10C. In Fig. 10B, following local histogram equalization and binary segmentation, the fractal dimension was calculated for each plaque component using the box-counting method. Initial results suggest that the fractal dimensions for lipid-pools, fibrous caps, and calcifications distinguish these tissue types. Finally, as described in Eq. 1, the OCT signal is a function of the tissue reflectance multiplied by a depth-dependent exponential decay. When a logarithm is applied to the OCT signal,

$$\ln[I(z)] = \ln[I_0] + \ln[R(z)] - 2\mu_t(z)z \quad \text{Eq. 2}$$

the exponential decay becomes a change in slope, $-2\mu_t(z)$, which is also known as the depth dependent total attenuation coefficient. In a preliminary study, we have measured $\mu_t(z)$, and have found that it is different for calcifications, fibrous caps, and
 5 lipid pools.

The present invention provides an algorithm for calculating $\mu_t(z)$ for each point in the image using adaptive linear regression to create new images that represent corrected total attenuation coefficients and corrected reflection coefficients that will provide improved characterization of tissue constituents. The algorithm is as follows:

- 10 (1) Identifying of the surface of the tissue at given transverse position, θ_0 ;
- (2) Selecting a small ROI (e.g., 7 x 1 pixels) within the radial scan, centered at r_0 , θ_0 ;
- (3) Smoothing operation over the ROI (e.g., linear filter);
- (4) Fitting the slope of the axial reflectivity within the ROI; and,
- 15 (5) Mapping the slope to total attenuation coefficient and the y-intercept of the slope to corrected reflectivity for r_0 , θ_0 (using more superficial total attenuation coefficients to compensate for the decrease in fluence at the current depth).

Steps 2-5 are repeated for the entire image.

POLARIZATION

Polarization sensitive optical coherence tomography is capable of improving the characterization of the composition of atherosclerotic plaques. With this device, quantitative high-resolution depth-resolved detection of plaque birefringence (polarization rotation by the tissue) gives rise to additional information related to plaque composition.

Fig. 11 shows a schematic of a polarization sensitive OCT system 100 according to one embodiment of the present invention. A polarized source (e.g., s state) 102 is incident on a 90/10 beam splitter 104 (BS). Light is directed to the reference arm 106 and sample arm 108 of the interferometers 110 via circulators 112 (C, port 1 to port 2 to port 3), and recombined by a 90/10 beam splitter 114. The s and p states of the recombined light are directed to detectors A and B (116, 118), respectively by a polarizing beam splitter 120 (PBS).

A polarization independent OCT image may be obtained by summing the squares of the magnitude of the interference detected at detectors A and B. If the polarization eigenstates of the electric field incident on the sample are known, then the birefringence of the sample may be computed using a combination of the signals detected by A and B. This is termed polarization sensitive detection. One quantitative measurement of the relative degree of birefringence caused by the sample is:

$$\phi(r, \theta) = \arctan\left(\frac{A(r, \theta)}{B(r, \theta)}\right) \quad \text{Eq. 3}$$

By analyzing the birefringence, additional information can be obtained from the OCT signal. Figs. 12A and B show OCT images of human coronary artery plaque acquired in vivo. Fig. 12A is a polarization independent image showing the presence of a

fibrous plaque from 11 o'clock to 8 o'clock (clockwise). Fig. 12B is a polarization sensitive image showing presence of bands (arrows) within the fibrous plaque.

In the polarization independent image (Fig. 12 A), the coronary plaque appears as a homogeneous signal-rich region which obliterates the normal layered structure of the artery. Fig. 12B shows the birefringence image ($\phi(r, \theta)$) of the same plaque. Radial bands are seen within the lesion, representing rotation of the polarization by the sample through several phases of the arctangent. The existence of these bands suggests that this plaque contains abundant, regularly oriented collagen fibers. A less stable plaque with a decreased collagen content should not show this banding structure.

Collagen content is the major intrinsic factor contributing to the stability of a plaque. As a result, a method for measuring the collagen content and its structural orientation will provide additional diagnostic information for differentiating stable from unstable plaques. Also, since an increase in plaque collagen content has been recognized as one of the most important structural changes that occurs following lipid-lowering therapy, measurement of the collagen content with this technique could enable monitoring of plaque regression after pharmacological therapy. In addition, the polarization sensitive OCT signal may improve the capability of OCT to differentiate lipid from fibrous tissue and fibrous tissue from calcium. Finally, other constituents commonly found in atherosclerotic plaques, such as cholesterol crystals, may have a unique polarization sensitive OCT signal.

Figs. 13A-C show images taken using polarization sensitive OCT. Fig. 13A is an OCT polarization diversity image; Fig. 13B is a polarization sensitive image; and, Fig. 13C is the histology of the same site. There is a difference between the

polarization birefringence for lipid and adjacent collagen. In the polarization sensitive image one can see that there is banding which means rotation of the polarization state (indicated by the arrow). In addition the lipid pool randomly alters the polarization state showing a very homogeneous speckle pattern in Fig. 13B. The fibrous tissue shows a banding pattern. Experimental results have also shown that calcifications, which at times may be very difficult to distinguish from lipid, do not have random alterations in returned polarization and are also not birefringent.

Macrophage Measurement

Example 1 discussed hereinbelow provides a method and an algorithm for identifying macrophages in fibrous caps.

EXAMPLES

Example 1

This example was a project to explore the potential of OCT for identifying macrophages in fibrous caps of atherosclerotic plaques.

Specimens

264 grossly atherosclerotic arterial segments (165 aortas, 99 carotid bulbs) were obtained from 59 patients (32 male and 27 female, mean age 74.2 ± 13.4 years) at autopsy and examined. 71 of these patients had a medical history of symptomatic cardiovascular disease (27.1%). The harvested arteries were stored immediately in phosphate buffered saline at 4°C . The time between death and OCT imaging did not exceed 72 hours.

OCT Imaging Studies

The OCT system used in this Example has been previously described. OCT images were acquired at 4 frames per second (500 angular pixels x 250 radial pixels), displayed with an inverse gray-scale lookup table, and digitally archived. The optical source used
5 in this experiment had a center wavelength of 1310 nm and a bandwidth of 70 nm, providing an axial resolution of approximately 10 μm in tissue. The transverse resolution, determined by the spot size of the sample arm beam, was 25 μm .

Before OCT imaging, arteries were warmed to 37°C in phosphate buffered saline. Each carotid bulb and aorta was opened and imaged with the luminal surface exposed. The
10 position of the interrogating beam on the tissue was monitored by a visible light aiming beam (laser diode, 635 nm) that was coincident with the infrared beam. Precise registration of OCT and histology was accomplished by applying ink marks (Triangle Biomedical Sciences, Durham, NC) to the vessels at the imaging site, such that each OCT image and corresponding histologic section contained visually recognizable
15 reference points.

Staining

After imaging, the tissue was processed in a routine fashion. Arterial segments were fixed in 10 % Formalin (Fisher Scientific, Fair Lawn, NJ) for at least 48 hours. Arteries with substantial calcification were decalcified (Cal-EX, Fisher Scientific) prior to
20 standard paraffin embedding. Four-micron sections were cut at the marked imaging sites and stained with hematoxylin and eosin (H&E) and Masson's trichrome. To visualize the presence of macrophages and smooth muscle cells, a mouse-antihuman CD68 monoclonal antibody and alpha-actin monoclonal antibody (Dako Corporation, Carpinteria, USA) were used, respectively. Immunohistochemical detection of the

preferred epitopes was performed according to the indirect horseradish peroxidase technique. After blocking with horse serum, the tissue was incubated with primary antibodies followed by horse anti-mouse secondary antibody and streptavidin with peroxidase (BioGenex) for anti-smooth muscle actin or avidin-biotin horseradish peroxidase complex (Dako) for anti-CD68. Slides were developed with 3-amino-9-ethyl-carbazole (Sigma) and counterstained with Gill's hematoxylin (Fisher Scientific). All slides were digitized for histomorphometric analysis (Insight Camera, Diagnostic Instruments, Sterling Heights, Michigan).

Correlation between OCT Images and Histopathology

264 OCT images and correlating histologic sections were obtained using the ink marks as points of reference. From this set, 26 plaques identified as fibroatheromas by histology with precise registration between OCT and histology as determined by reference ink marks and minimal superficial calcification by histology, were selected to correlate measurements of macrophage density.

Morphometric analysis

Using both digitized histology and OCT, measurements of macrophage density were obtained using a 500 x 125 μm (lateral x axial) region of interest (ROI), located in the center of the plaque (Fig. 1). For caps having a thickness less than 125 μm , the depth of the ROI was matched to the cap thickness.

OCT measures the intensity of light returning from within a sample. Samples having a higher heterogeneity of optical index of refraction exhibit stronger optical scattering and therefore a stronger OCT signal. If the characteristic size scale of the index of refraction heterogeneity is larger than the resolution, then the OCT signal will have a larger

variance. Previous research conducted to measure the optical properties of human tissue has shown that the refractive index of lipid and collagen is significantly different. These results suggest that caps containing macrophages should have multiple strong backreflections, resulting in a relatively high OCT signal variance. Using standard
 5 image processing methods, the variance, σ^2 , within the ROI of an OCT image can be represented by:

$$\sigma^2 = \frac{1}{N-1} \sum_{ROIwidth} \sum_{ROIheight} (S(x,y) - \bar{S})^2, \quad \text{Eq. 4}$$

where N is the number of pixels in the ROI, $ROIwidth$ is the width of the ROI, $ROIheight$ is the height of the ROI, $S(x,y)$ is the OCT signal as a function of x and y
 10 locations within the ROI, and \bar{S} is the average OCT signal within the ROI.

OCT images contain tissue backreflection information that span a large dynamic range (100 dB or 10 orders of magnitude). The dynamic range of OCT is too high to be displayed on a standard monitor that may have a dynamic range of only 2-3 orders of magnitude. As a result, the signal range of most OCT images are compressed by taking
 15 the base 10 logarithm of the OCT image prior to display. While taking the logarithm of the OCT image data enables convenient image display, compression of the data range in this manner diminishes image contrast. In this study, we investigated the capabilities of both the raw (linear) OCT data and the logarithm of the OCT data for quantifying macrophage content within fibrous caps.

20 Prior to computing the image standard deviation, the OCT data within the ROI was preprocessed using the following steps: 1) the mean background noise level was

subtracted, and 2) median filtering using a 3x3 square kernel was performed in order to remove speckle noise (IPLab Spectrum 3.1, Scanalytics, Vienna, VA). Following preprocessing, σ within the ROI was calculated and tabulated for each specimen. In order to correct the data for variations in OCT system settings, σ was normalized by the
 5 maximum and minimum OCT signal present in the OCT image:

$$NSD = \frac{\sigma}{(S_{\max} - S_{\min})}, \quad \text{Eq. 5}$$

where NSD is the normalized standard deviation of the OCT signal, S_{\max} is the maximum OCT image value, and S_{\min} is the minimum OCT image value.

The area percentage of CD68+ and smooth muscle actin staining was quantified (at
 10 100x magnification) using automatic bimodal color segmentation within the corresponding ROI's of the digitized Immunohistochemical stained slides (IPLab Spectrum 3.1, Scanalytics, Vienna, VA). The NSD within each cap was then compared with immunohistochemical staining from slides obtained from corresponding locations.

Statistics

15 OCT measurements of macrophage and smooth muscle density were compared to histologic measurements using linear regression. In addition, following retrospective application of an NSD threshold, the accuracy of OCT for identifying caps with > 10% CD68+ staining was determined. All continuous variables are expressed as mean \pm standard deviation. A p value < 0.05 was considered statistically significant.

Results

Macrophage Density

The OCT signal within the cap is relatively homogeneous for low macrophage density, whereas for high macrophage content, the OCT image of the cap is heterogeneous with punctate, highly reflecting regions. The relationship between macrophage density determined by immunohistochemistry and the NSD measured by OCT is depicted in Fig. 14 for both the raw and base 10 logarithm OCT data. For the raw OCT data, a correlation of $r = 0.84$ ($p < 0.0001$) was found between OCT NSD and CD68+% staining, whereas for the base 10 logarithm OCT data, a correlation of $r = 0.47$ ($p < 0.05$) was found between OCT NSD and CD68+% staining.

Morphometric evaluation of 26 slides stained with CD68 showed 9 caps with a CD68+ area greater than 10% and 17 caps with a CD68+ area less than 10%. Receiver operating characteristic (ROC) curves for the raw and base 10 logarithm OCT signal NSD's are depicted in Fig.4. For the raw OCT signal NSD, a range of NSD's (6.15% - 6.35%) demonstrated 100% sensitivity and specificity (\square value 1.0) for differentiating caps containing $> 10\%$ CD68+ staining. For the base 10 logarithm OCT signal, NSD values ranging from 7.65% - 7.75% provided 70% sensitivity and 75% specificity (\square value 0.44) for identifying caps containing $> 10\%$ CD68+ staining. A comparison of the OCT NSD and CD68+ staining is summarized in Table 3. CD 68+% staining cutoff 10%. Data in parenthesis represents 95% confidence interval. OCT - Optical Coherence Tomography; NSD - Normalized Standard Deviation of OCT signal.

Table 3

	Raw OCT Signal	Logarithm OCT signal
Correlation (r)	0.84 (p<0.0001)	0.47 (p < 0.05)
NSD Cutoff	6.2%	7.7%
Sensitivity	1.0 (0.69-1.0)	0.70 (0.35-0.93)
Specificity	1.0 (0.8-1.0)	0.75 (0.48-0.93)
Positive Predictive Value	1.0 (0.69-1.0)	0.64 (0.3-0.89)
Negative Predictive Value	1.0 (0.8-1.0)	0.80 (0.52-0.96)

Smooth Muscle Cell Density

A negative correlation was found between CD68 and smooth muscle actin % area staining (r = -0.44, p < 0.05). In turn, a statistically significant negative relationship between smooth muscle cell density determined by immunohistochemistry and OCT NSD was observed for both the raw and base 10 logarithm OCT data. For the raw OCT data, a correlation of r = -0.56 (p < 0.005) was found between OCT NSD and smooth muscle actin+% staining, whereas for the base 10 logarithm OCT data, a correlation of r = -0.32 (p = 0.12) was found between OCT NSD and smooth muscle actin+% staining.

Other Findings

Macrophages at the cap-lipid pool interface: CD68 staining demonstrated a significant accumulation of macrophages at the cap-lipid pool interface in (n=19) cases. In 16 of these cases (84%), a higher OCT signal was also present at the junction between the cap and the lipid pool, confirming that the increase in OCT signal was in part due to increased backreflection by macrophages at the cap-lipid pool interface. For the three CD68+ cases lacking an increase in OCT signal at the junction, either the cap was greater than 300 μ m in thickness or the entire cap was infiltrated by macrophages. In the three cases that were negative for CD68 at the cap-lipid pool interface, an increased OCT interface signal corresponded to cholesterol crystals present at the junction.

Although many new approaches under investigation for plaque characterization show great promise, none provide direct evidence of macrophage presence. This Example demonstrates that OCT is capable of visualizing macrophages and quantifying cap macrophage content. Since the OCT signal increases with the number of refractive index mismatches in tissue, caps containing macrophages should have multiple strong backreflections. A simple computational analysis of ROI's within OCT images of fibrous caps (NSD) was developed to test this hypothesis. When validated against immunohistochemistry, this parameter demonstrated a high degree of correlation with CD68 staining at corresponding locations ($r = 0.84$ for raw OCT data NSD).

While little is known about the precise relationship between cap macrophage density and plaque vulnerability, studies have shown that plaques with a macrophage content in the range of 10% – 20% are more likely to be associated with unstable angina and non-Q wave myocardial infarction⁶. As a result, we selected 10% CD68+ area as a cutoff for high macrophage content. Using the ROC to select an appropriate NSD threshold, we found that OCT was capable of accurately distinguishing fibrous caps with low macrophage content from fibrous caps with high macrophage content (100% sensitivity and specificity for raw OCT data NSD).

An increased number of smooth muscle cells have been observed within plaques in patients who have unstable angina and within erosive plaques implicated in a subset of acute myocardial infarctions. In this work, we found an inverse correlation between CD68 and smooth muscle actin staining from corresponding locations within plaque caps ($r = -0.44$, $p < 0.05$). The negative correlation between the raw OCT data NSD and smooth muscle actin staining ($r = -0.56$, $p < 0.005$) may in part reflect the inverse relationship between macrophages and smooth muscle cells in our data. Nevertheless, it

appears that the OCT NSD is specific for macrophage content, as opposed to being a more general metric of increased cellular density.

In this Example, both the raw OCT signal and the logarithm of the OCT signal was processed and compared with CD68 immunohistochemical positivity. While the logarithm of the OCT signal provides an increased dynamic range for image display, it also apparently decreases the contrast between macrophages and surrounding matrix (Table 3).

Alternative Methods for Identifying Inflammation in Atherosclerotic Plaques

Diffuse near-infrared (NIR) reflectance spectroscopy is a quantitative approach that utilizes the spectrum of light scattered from within the vessel wall. A recent study, performed on cadaver specimens, has demonstrated that chemometric analysis of the NIR spectrum may allow identification of plaques containing abundant inflammatory cells. Based on the hypothesis that local inflammation within vulnerable plaques may lead to local elevations in temperature, studies have recently been performed using a temperature-sensing catheter. Experiments performed in patients have indicated that both temperature heterogeneity and the temperature difference between atherosclerotic plaque and healthy vessel walls increase with disease severity. Both NIR spectroscopy and thermography appear quite promising for assessing inflammation within plaques, but these diagnostic techniques are not specific for macrophages and may need to be combined with another imaging modality to precisely determine whether or not the inflammatory cells are confined to the fibrous cap, or are present throughout the plaque. Recently, ultrasmall superparamagnetic particles of iron oxide (USPIOs) have been proposed for delineation of inflammatory changes accompanying atherosclerotic

disease. The limited resolution of MRI, however, renders the localization of macrophages within thin fibrous cap and plaque shoulders difficult.

Alternative algorithms and methods:

In addition to the algorithm described hereinabove in Example 1, the following
5 alternative embodiments for determining macrophage content could also be employed:

Any combination of the techniques described below could be used in an algorithm for determining macrophage density

Focus Tracking

Precise knowledge of the position of the focus of the imaging lens may be needed for
10 accurate quantification. This may be accomplished by determining the maximum axial OCT signal or by *a priori* knowledge of the position of the focus on the OCT image.

Correction of Focus

The OCT image may be corrected to form a map of the true backscattering coefficient by an adaptive correction for the attenuation coefficient and extrapolation using 1xn
15 kernels in the OCT image. The resultant image would be a map of the true backscattering coefficients, corrected for attenuation.

Intensity normalization

1. Calibration of the OCT system prior to imaging using a known reflectance standard.
Alternatively, the normalization may occur within the image where the region of
20 interest for macrophage density determination is normalized to an adjacent region with homogeneous backscattering, presumably representing acellular fibrous tissue.

2. ROI's and/or Images are normalized by the calibration data so that the backscattering coefficient data is absolute.

Computation of macrophage density within ROI

- (1) Global ROI mean, variance, standard deviation, skew
- 5 (2) Fourier transform high frequency energy
- (3) Local variance, standard deviation
- (4) Segmentation and blob number or area counting
- (5) Edge density
- (6) Spatial gray level co-occurrence matrix parameters
- 10 (7) Fractal dimension
- (8) Run-length measurements

Cluster analysis or threshold application

Cluster analysis or threshold application may be needed to separate out plaques or ROI's with high macrophage content versus low macrophage content.

- 15 It will be understood that the terms “a” and “an” as used herein are not intended to mean only “one,” but may also mean a number greater than “one.” All patents, applications and publications referred to herein are hereby incorporated by reference in their entirety. While the invention has been described in connection with certain embodiments, it is not intended to limit the scope of the invention to the particular
- 20 forms set forth, but, on the contrary, it is intended to cover such alternatives, modifications, and equivalents as may be included within the true spirit and scope of the invention as defined by the appended claims.

CLAIMS

CLAIMED IS:

1. An apparatus for characterizing atherosclerotic plaque, comprising:
 - a. a housing
 - 5 b. a probe comprising:
 - i) at least one optic fiber,
 - ii) means for creating rotation of said fiber,
 - iii) at least one lens,
 - iv) at least one prism,
 - 10 v) at least one detector,
 - vi) a light source;
 - c. means for obtaining reflectance; and,
 - d. means for comparing the optical properties to a stored database of typical optical properties for a given tissue type and associated abnormalities.

2. A method for determining the thickness of a cap overlying a solid or liquid pool, comprising:
 - a. performing Monte Carlo simulations varying cap and lipid pool optical properties and cap thicknesses;
 - 5 b. developing a lookup table of Monte Carlo results;
 - c. performing spatial reflectance distribution measurements for N wavelengths;
 - d. fitting the measured spatial reflectance distribution to known Monte Carlo simulation results (e.g., by the Levenberg-Marquardt method); and,
 - e. outputting the optical properties and cap thickness from the previously
10 computed Monte Carlo simulation that closely approximates the experimental measurements.
3. The method of Claim 2, wherein the Levenberg-Marquardt method is used to fit the measured spatial reflectance distribution.

4. A method of characterizing the thickness of a cap overlying a liquid or solid pool, comprising:
 - a. directing a beam of light onto the surface of a sample;
 - b. detecting the light reflected from said surface;
 - 5 c. determining the decay and broadening of said pulse reflected from said surface, said decay comprising a first curve due to the optical properties of said cap and a second curve due to the optical properties of said liquid or solid pool;
 - d. measuring the effective attenuation coefficient $\mu_{\text{eff}} = 1/[3\mu_s(\mu_s + \mu_a)]$ or the total attenuation coefficient, $\mu_t = \mu_s + \mu_a$, where μ_t is the total scattering coefficient, 10 μ_a is the absorption coefficient, and μ_s is the scattering coefficient;
 - e. measuring the thickness of said cap by determining the cutoff region where the exponential decay changes.
5. The method of Claim 4, wherein said beam of light is a short temporal pulse.
- 15 6. The method of Claim 4, wherein said beam of light is an oscillating beam of light in at amplitude A_1 and out at amplitude A_2 , where a phase shift (ϕ) occurs between the two peaks and there is an amplitude decrease where $A_2 < A_1$.

7. A method of characterizing the thickness of a cap overlying a liquid or solid pool, comprising:
- a. directing a beam of light onto the surface of a sample;
 - b. detecting a first wavelength of light reflected from said sample;
 - 5 c. detecting a second wavelength of light reflected from said sample;
 - d. calculating the ratio of said first wavelength to said second wavelength; and,
 - e. determining the thickness of said cap by comparing said ratio to a database of known cap thicknesses.
8. A method of characterizing the thickness of a cap overlying a liquid or solid pool, comprising:
- a. identifying of the surface of the tissue at given transverse position, θ_0 ;
 - b. selecting a small region of interest (ROI) within the radial scan, centered at r_0 , θ_0 ;
 - c. smoothing operation over the ROI;
 - 15 d. fitting the slope of the axial reflectivity within the ROI; and,
 - e. mapping the slope to total attenuation coefficient and the y-intercept of the slope to corrected reflectivity for r_0 , θ_0 .
9. The method of Claim 8, further comprising repeating steps b.-e. for the entire image.
10. The method of Claim 8, wherein said smoothing operation uses a linear filter.

11. An apparatus for imaging a sample, comprising:
- a. a housing;
 - b. a polarized source of light;
 - c. a first beam splitter;
 - 5 d. a reference arm;
 - e. a sample arm;
 - f. at least one interferometer;
 - g. at least two circulators;
 - h. a second beam splitter;
 - 10 i. a polarizing beam splitter; and,
 - j. at least two detectors.

12. A method of characterizing the thickness of a cap overlying a liquid or solid pool, comprising:

- a. directing a beam of polarized light onto a sample;
- b. detecting the light reflected back from said sample using at least two
5 circulators;
- c. summing the squares of the magnitude of the interference detected at said at least two circulators;
- d. determining the birefringence of said sample using a combination of the signals detected by said at least two detectors.

10 13. The method of Claim 12, wherein the relative degree of birefringence is determined by the equation:

$$\phi(r, \theta) = \arctan\left(\frac{A(r, \theta)}{B(r, \theta)}\right),$$

where $(\phi(r, \theta))$ is the birefringence image.

14. A method of measuring macrophage presence or content in plaque, comprising:

- a. directing a beam of light onto the surface of a sample;
- b. detecting the light data reflected back from said surface;
- c. determining the index of refraction of said sample in a region of interest (ROI);
- d. subtracting the mean background noise level from said data;
- e. median filtering using a kernel in order to remove speckle noise;
- f. determining the standard deviation σ within said ROI; and,
- g. normalizing the maximum and minimum signal present in said data using the equation

$$NSD = \frac{\sigma}{(S_{\max} - S_{\min})}$$

where NSD is the normalized standard deviation of the OCT signal, S_{\max} is the maximum OCT image value, and S_{\min} is the minimum OCT image value

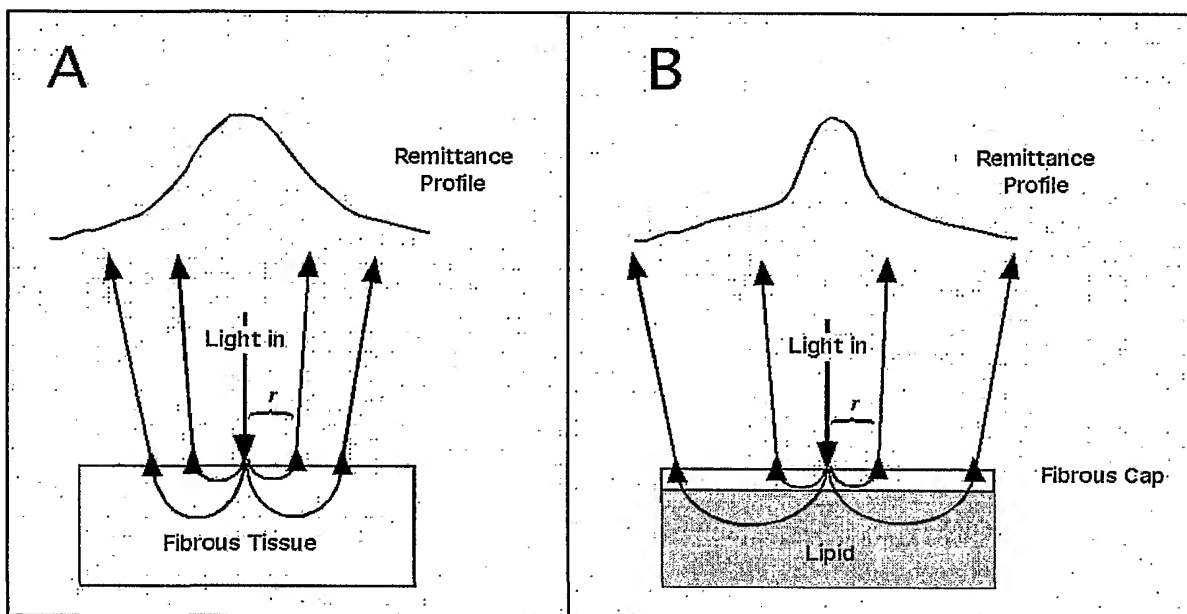


FIG. 1

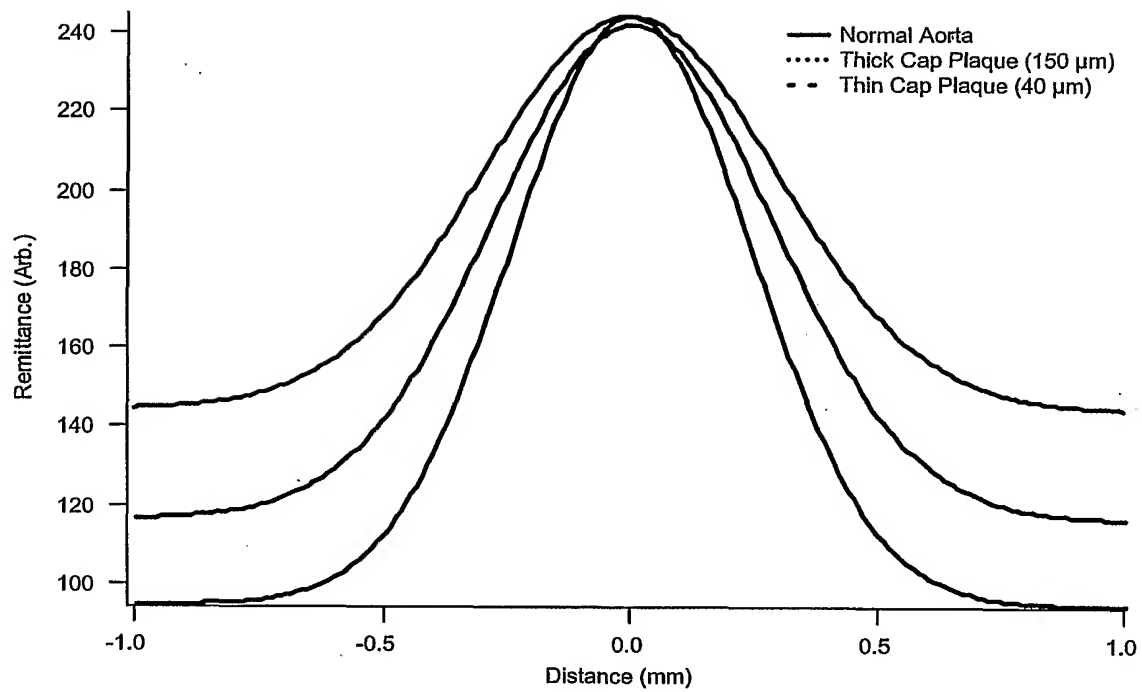
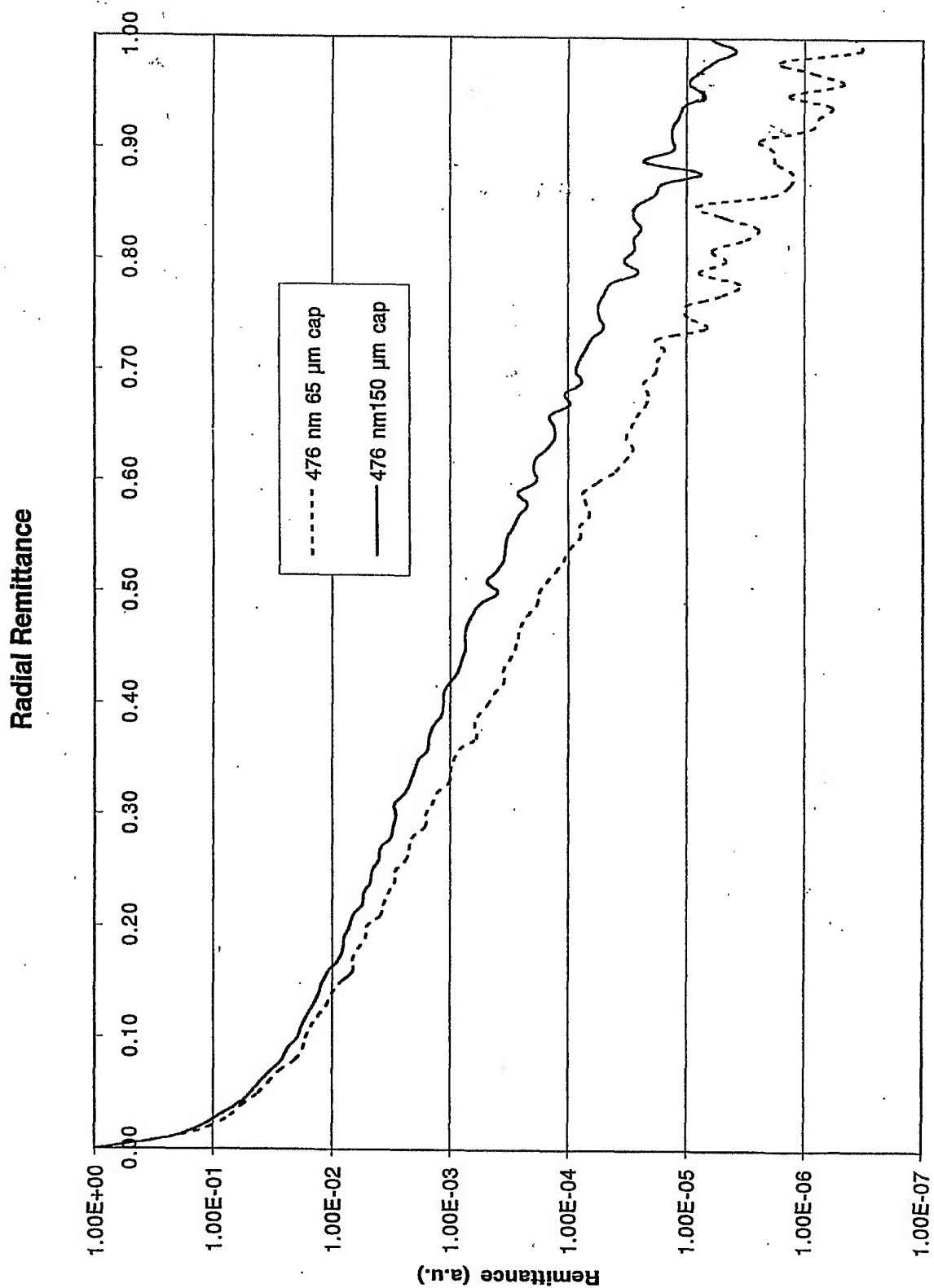


FIG. 2



r (mm)

FIG. 3

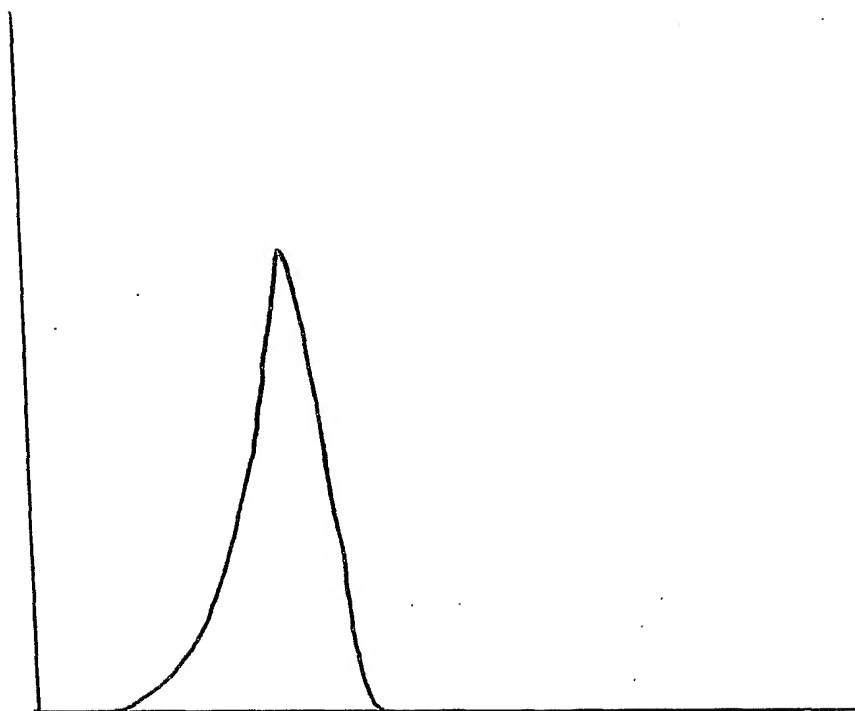


FIG. 4A

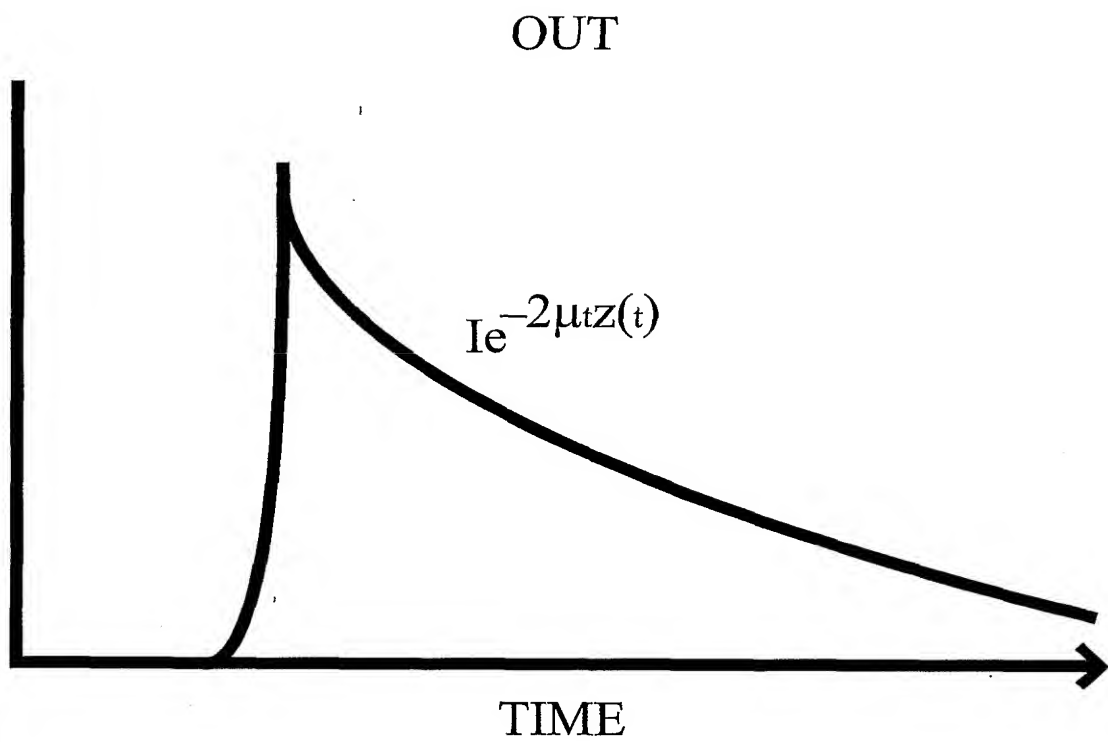


FIG. 4B

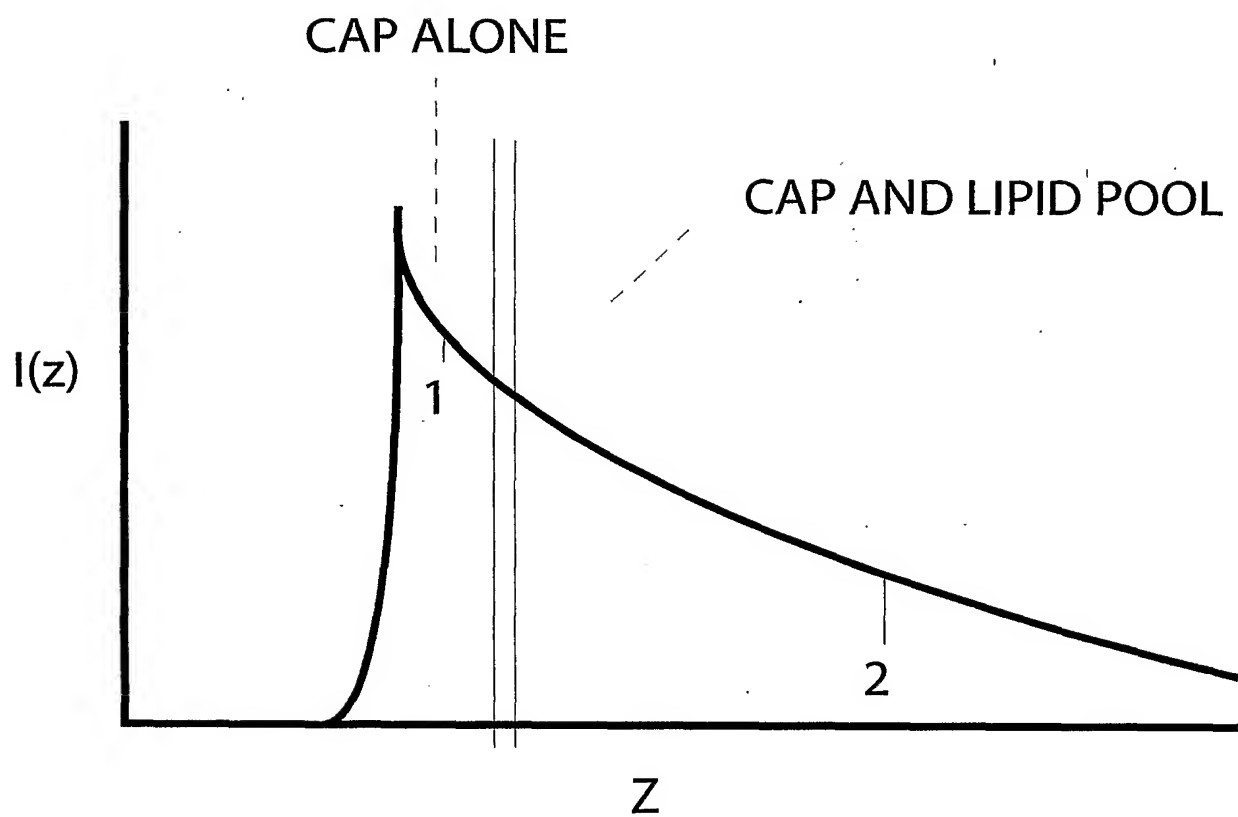


FIG. 4C

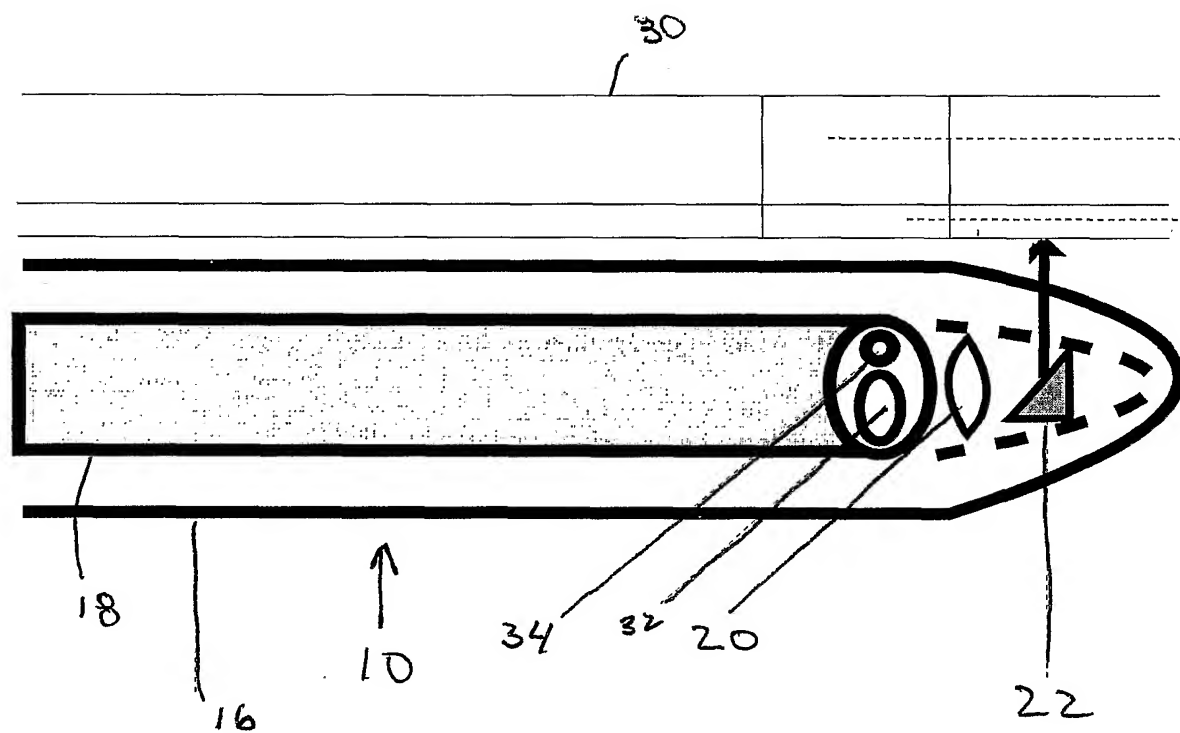


FIG. 5A

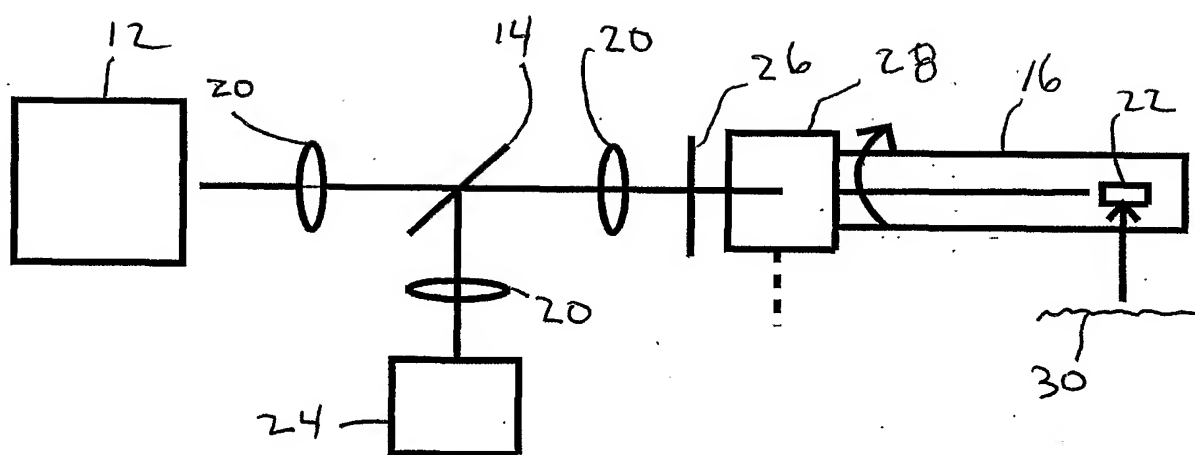


FIG. 5B

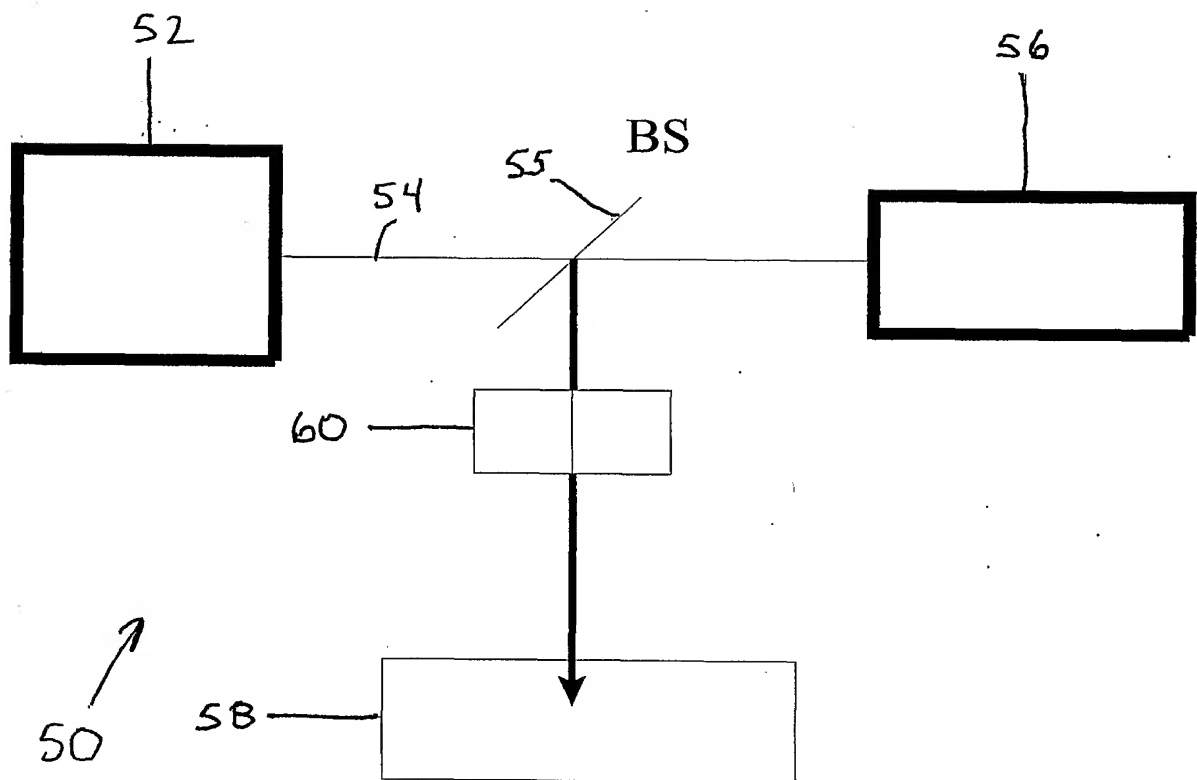


FIG. 5C

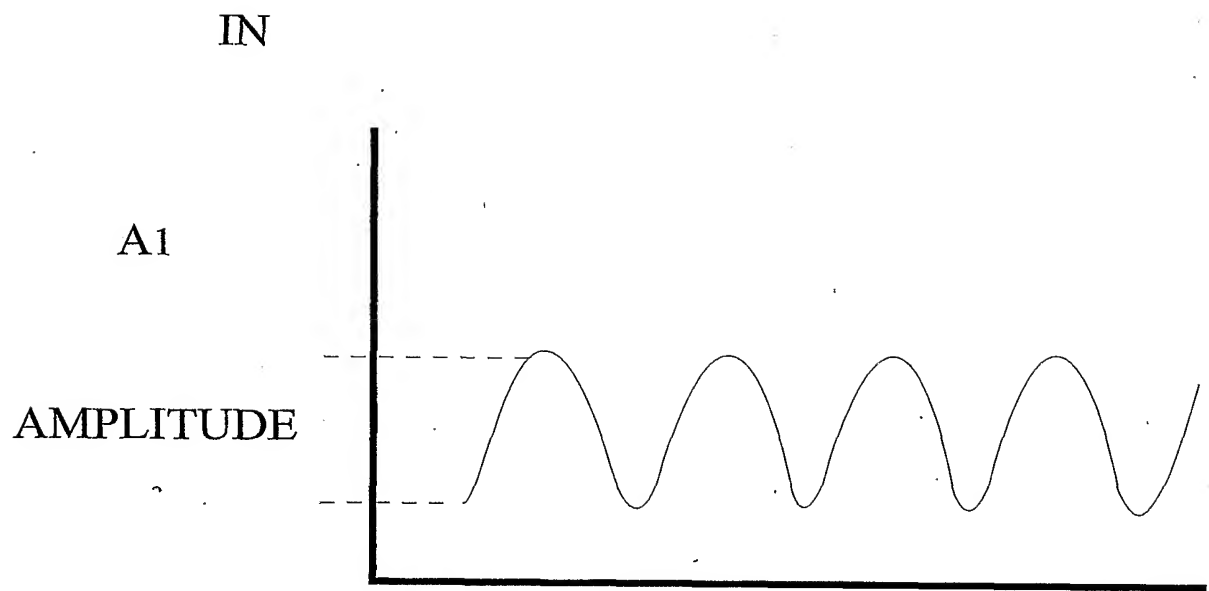


FIG. 6A

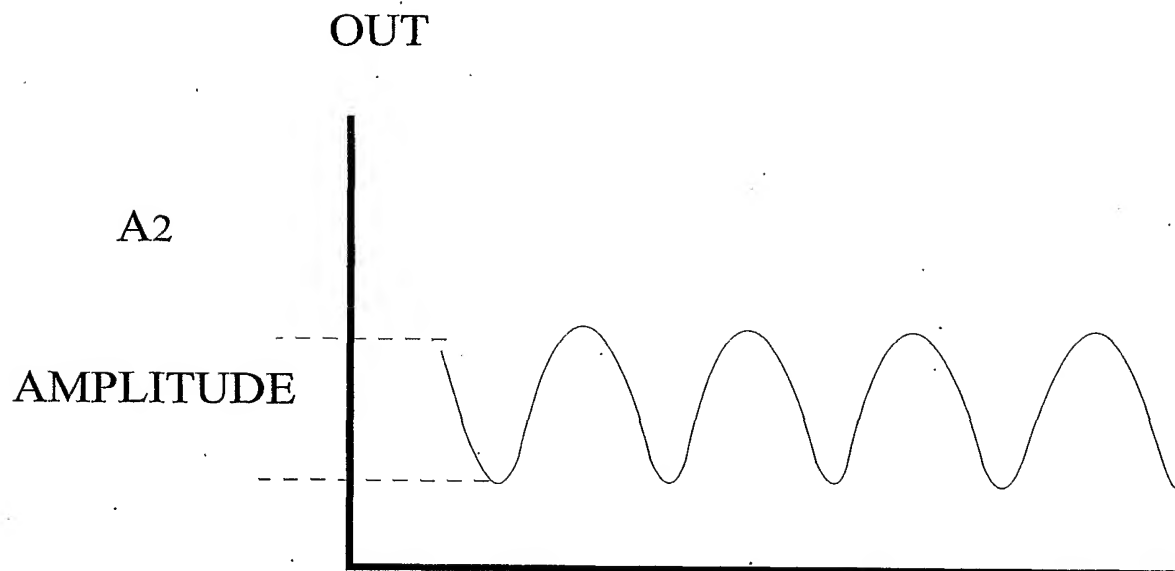


FIG. 6B

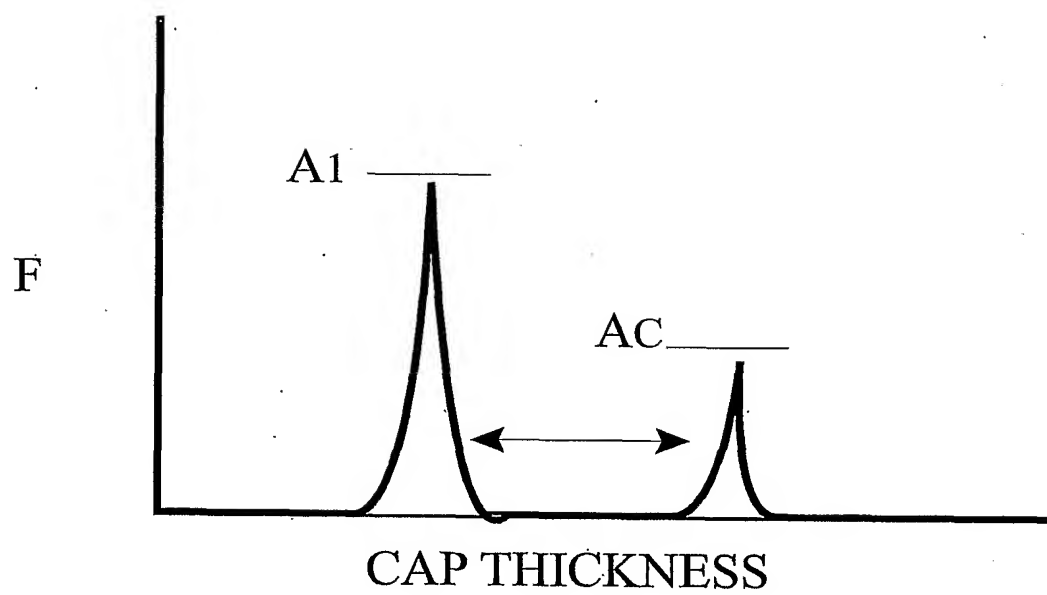


FIG. 7A

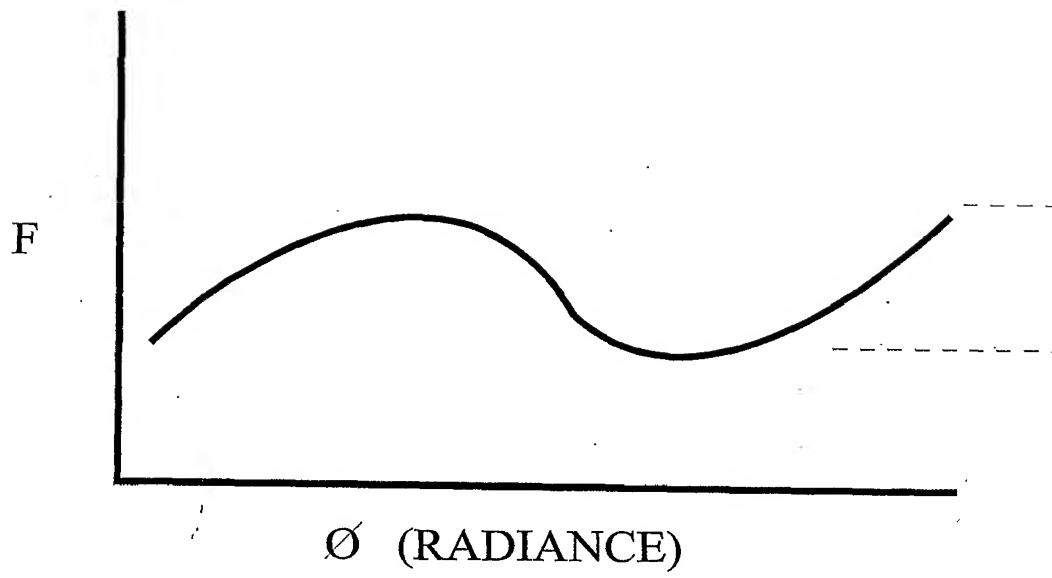


FIG. 7B

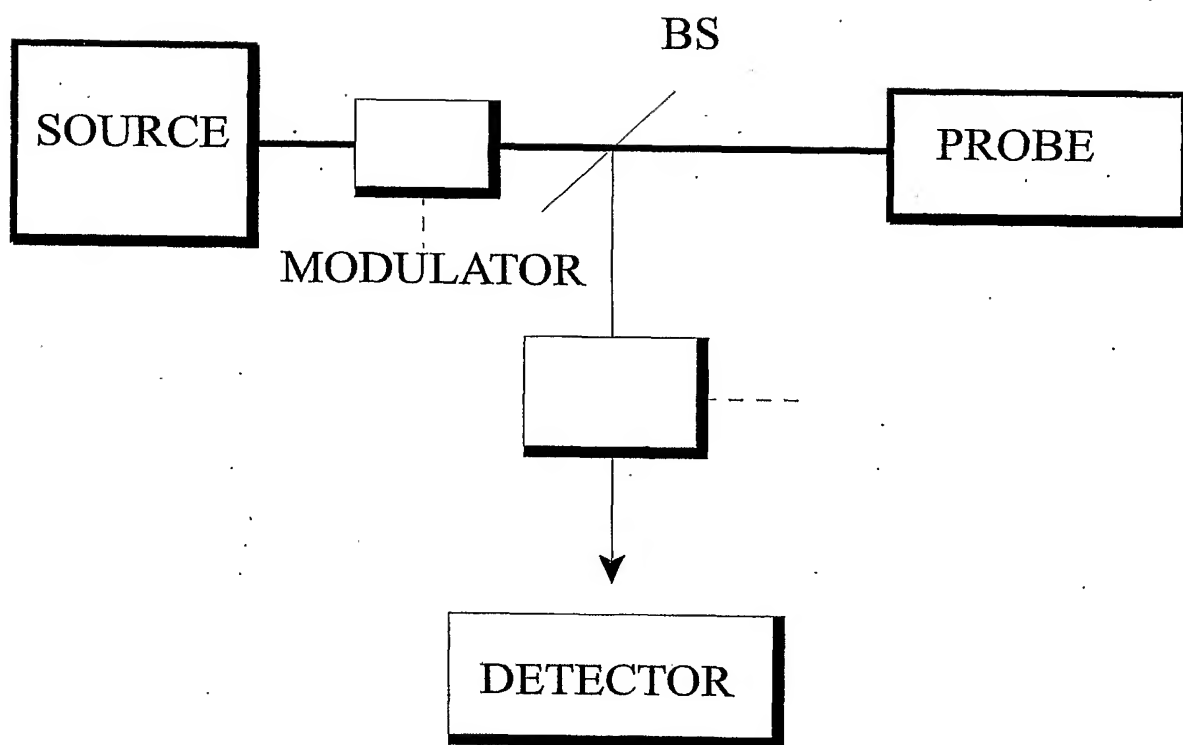


FIG. 8

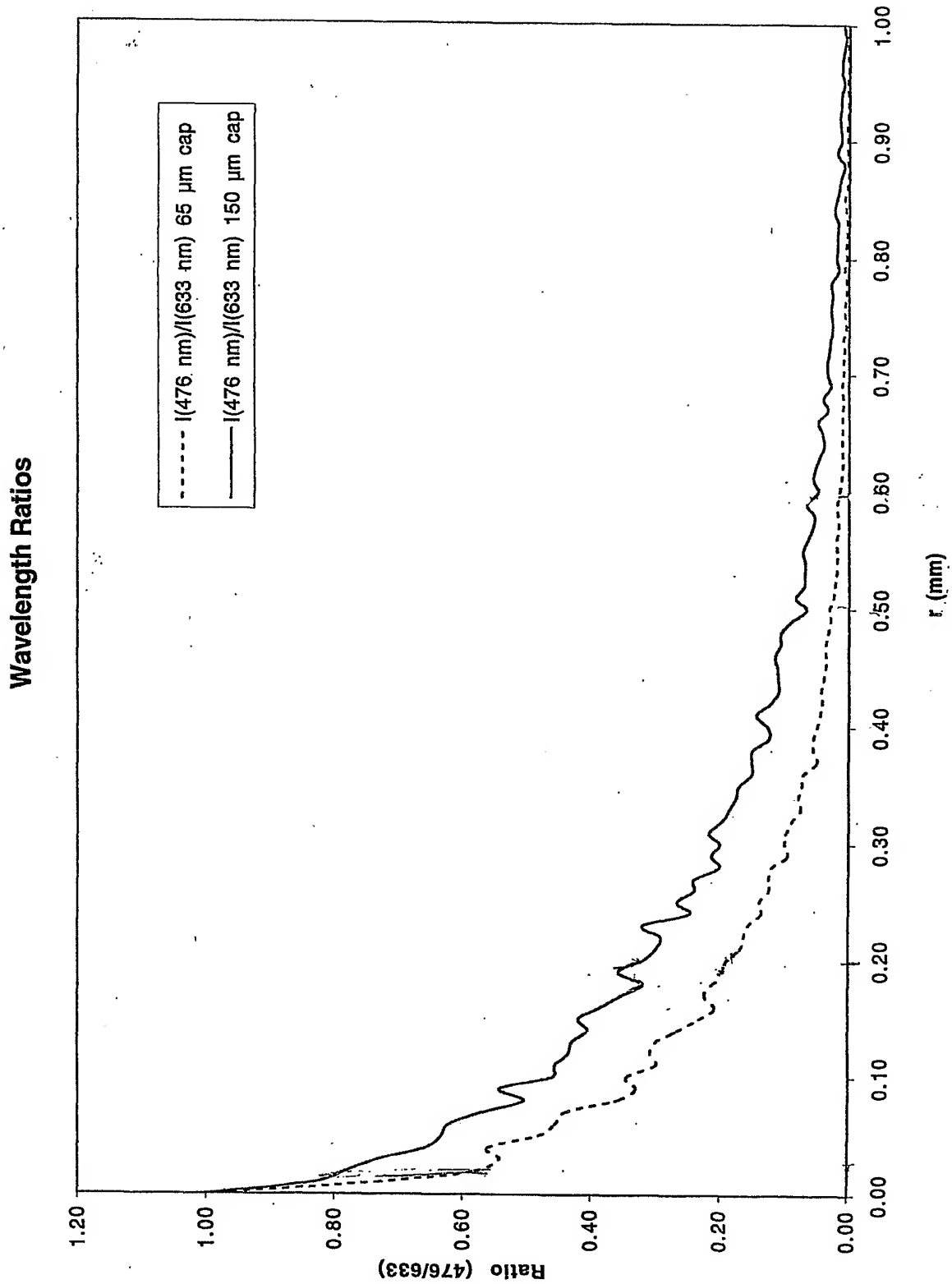


FIG. 9

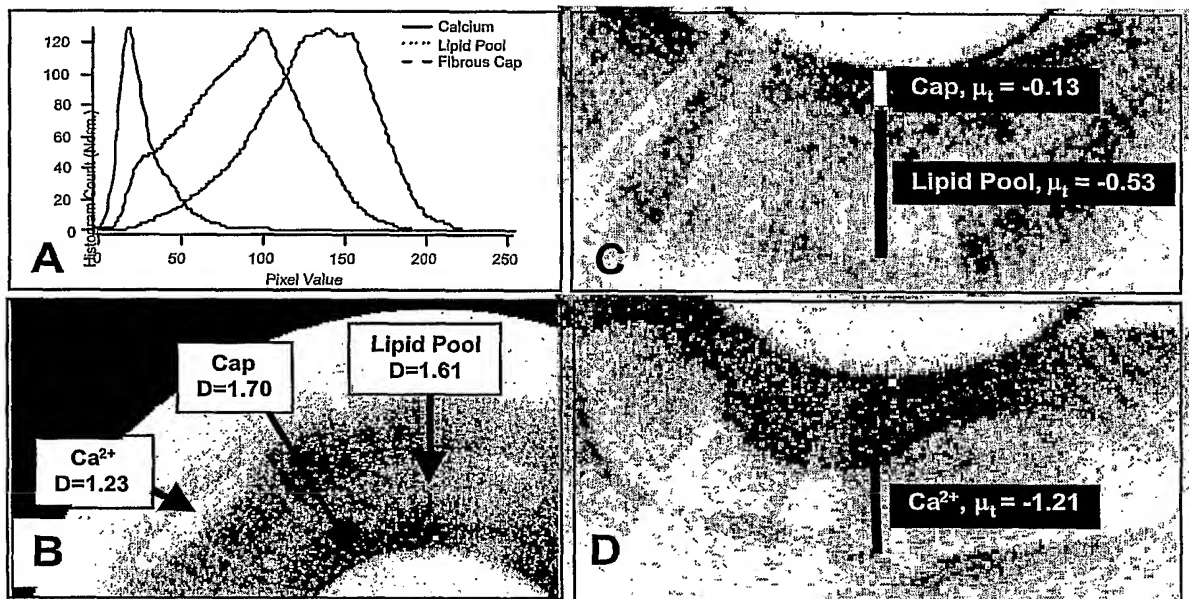


FIG. 10

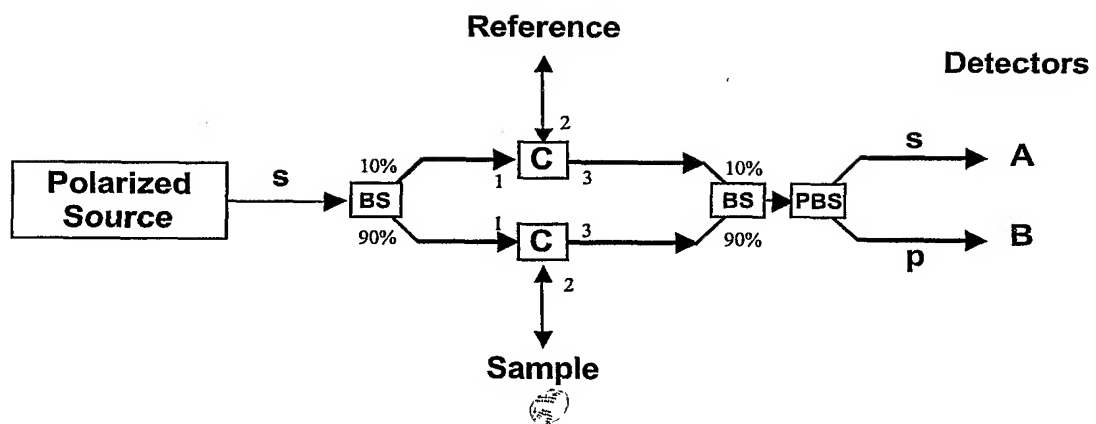


FIG. 11

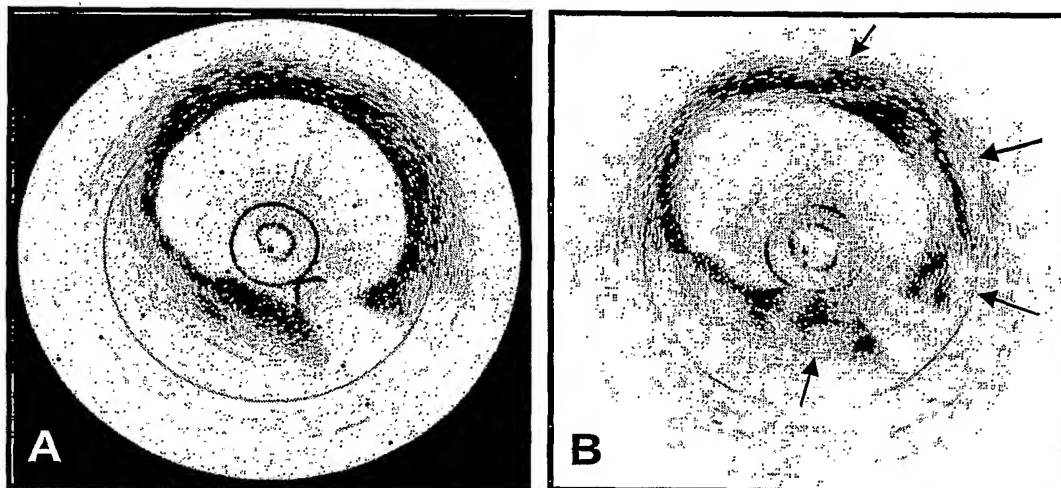


FIG. 12

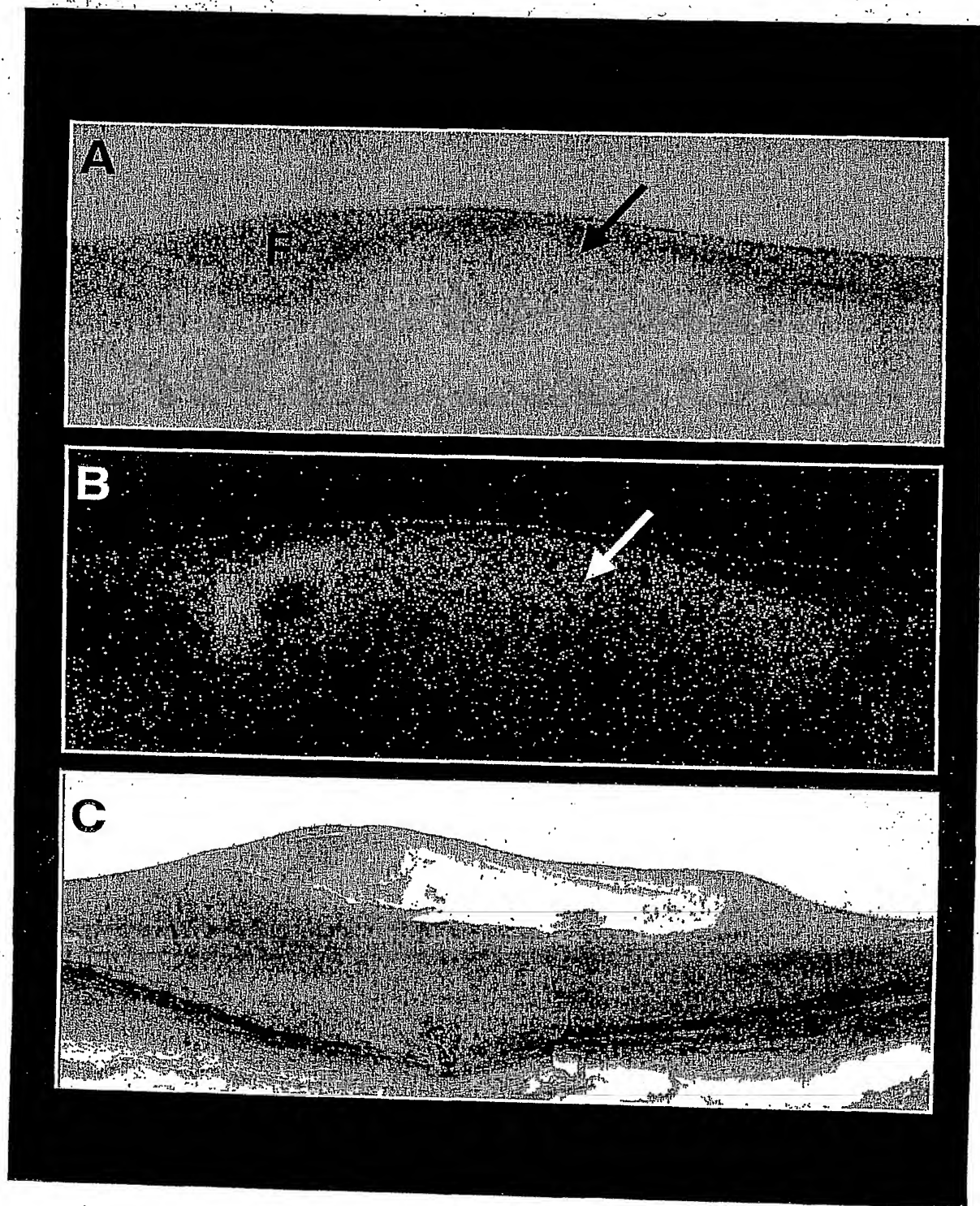


FIG. 13

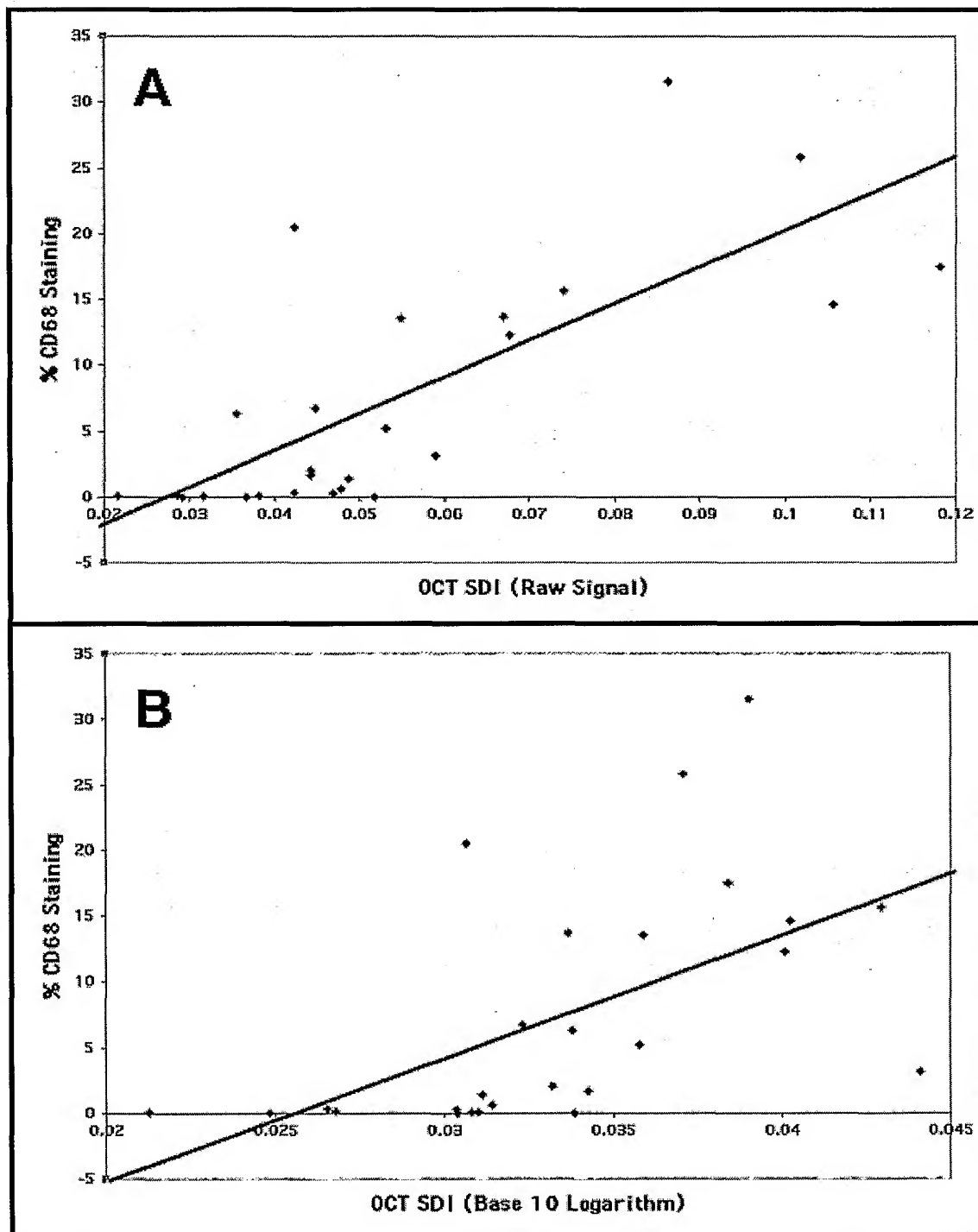


FIG. 14